

Pressure-Produced Ionization of Nonideal Plasma in a Megabar Range of Dynamic Pressures

V. E. Fortov^a, V. Ya. Ternovoĭ^a, M. V. Zhernokletov^b, M. A. Mochalov^b,
 A. L. Mikhailov^b, A. S. Filimonov^a, A. A. Pyalling^a, V. B. Mintsev^{a,*},
 V. K. Gryaznov^{a,**}, and I. L. Iosilevskii^c

^a*Institute for Chemical Physics Problems, Russian Academy of Sciences, Chernogolovka,
 Moscow oblast, 142432 Russia*

**e-mail: minv@icp.ac.ru*

***e-mail: grvkb@icp.ac.ru*

^b*Russian Federal Nuclear Center All-Russian Research Institute of Experimental Physics, Sarov,
 Nizhni Novgorod oblast, 607200 Russia*

^c*Moscow Institute for Physics and Technology (State University), Dolgoprudnyi,
 Moscow oblast, 141200 Russia*

Received January 29, 2003

Abstract—The low-frequency electrical conductivity of strongly nonideal hydrogen, helium, and xenon plasmas was measured in the megabar range of pressures. The plasmas in question were generated by the method of multiple shock compression in planar and cylindrical geometries, whereby it was possible to reduce effects of irreversible heating and to implement a quasi-isentropic regime. As a result, plasma states at pressures in the megabar range were realized, where the electron concentration could be as high as $n_e \approx 2 \times 10^{23} \text{ cm}^{-3}$, which may correspond to either a degenerate or a Boltzmann plasma characterized by a strong Coulomb ($\Gamma_D = 1\text{--}10$) and a strong interatomic ($\Gamma_a = r_a n_a^{1/3} \sim 1$) interaction. A sharp increase (by three to five orders of magnitude) in the electrical conductivity of a strongly nonideal plasma due to pressure-produced ionization was recorded, and theoretical models were invoked to describe this increase. Experimental data available in this region and theoretical models proposed by various authors are analyzed. The possibility of a first-order “phase transition” in a strongly nonideal plasma is indicated. © 2003 MAIK “Nauka/Interperiodica”.

1. INTRODUCTION

The behavior of plasma, which is the most widespread state of matter in nature, under the conditions of strong heating and compression is of considerable interest from the general physical point of view; it is also of practical interest for astrophysics, the physics of giant planets, and promising applications in power engineering [1–3]. Particular attention is being given to the ionization composition of a plasma, since this provides a basis for calculating its thermodynamic, transport, and optical properties.

It is well known that plasma can be obtained not only via strong heating up to temperatures commensurate with the ionization potential, $k_B T \sim I$, but also via a strong compression to a state in which the interparticle spacing becomes commensurate with atomic sizes, $r_a \sim n_a^{-1/3}$; the second way is referred to as cold ionization or pressure-produced ionization. While thermal-ionization processes have to date received quite adequate study [1], investigation of pressure-produced ionization is much more complicated since one deals here with a cold ($k_B T \ll I$) compression of a plasma to pressures in

the megabar range and densities that considerably exceed solid-state values. Under such conditions, the interaction between particles becomes strong (nonideality), the electron shells of atoms and molecules overlap, and the typical level of electrical conductivity is commensurate with that in metals. Frequently, such a regime is erroneously called metallization, even though Landau and Zeldovich [4], Mott and Davis [5], and Hensel and Frank [6] showed that a metal can be distinguished from a dielectric only by their electron spectra at $T = 0$ but not by the level of the electrical conductivity itself. By way of example, we indicate that dilute tokamak plasmas ($n_e \sim n_i \sim 10^{14} \text{ cm}^{-3}$, $T \approx 5\text{--}10 \text{ keV}$) have an electrical conductivity close to that of pure copper [7].

Implementing the isothermal expansion of low-boiling metals at supercritical pressures [6, 8], one can continuously pass from a high-conducting metallic state to low-conducting gaseous dielectric states and establish that a metal–dielectric transition occurs in a narrow range of densities that are close to (Cs, Rb, K) or somewhat greater (Hg) than the matter density at the critical point. For the majority of other metals, which constitute

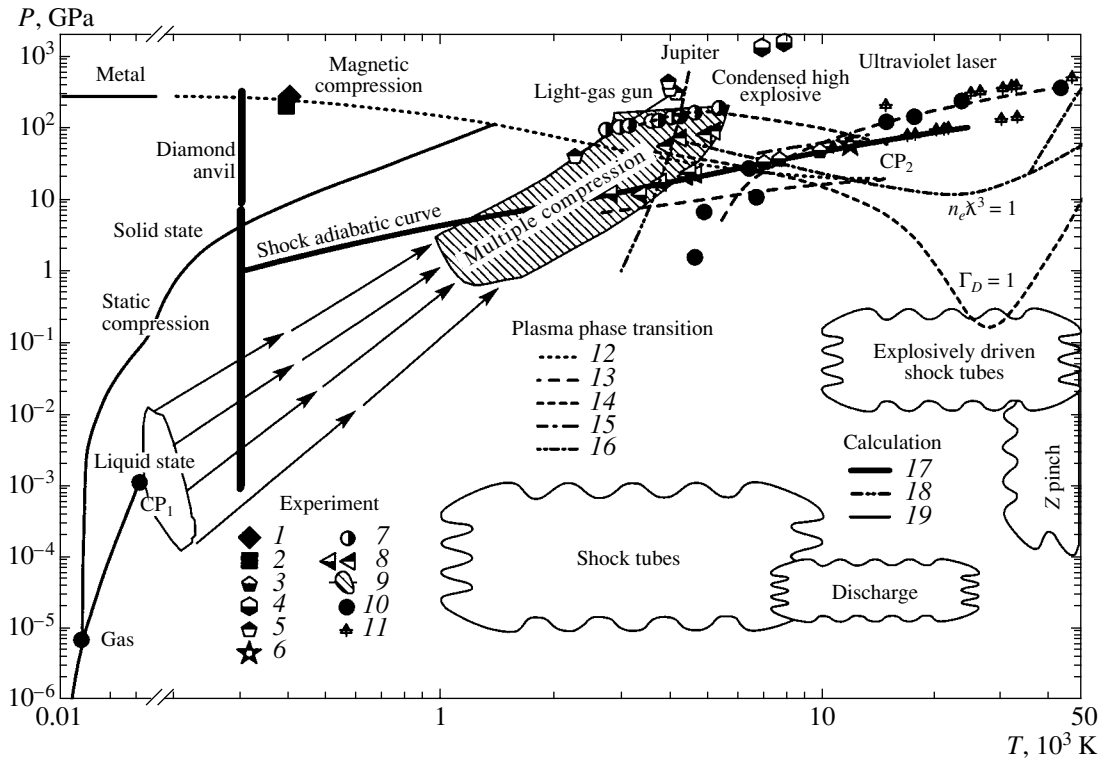


Fig. 1. Phase diagram of hydrogen. The displayed experimental data were obtained in (1, 2) magnetic compression [29, 30], (3) Z pinch [33], (4, 5) cylindrical compression [26, 27], (6) spherical compression [28]; (7, 8) single and multiple compression by means of a light-gas gun [34, 35], (9) multiple shock compression [36], and (10, 11) shock compression by a laser [31, 32]. The estimates for the critical point of the plasma phase transition in hydrogen were taken from the articles of (12) Beule *et al.* [37], (13) Robnic and Kundt [38], (14) Saumon and Chabrier [23], (15) Haronska *et al.* [39], and (16) Mulenka *et al.* [24]. The calculated data correspond to (17) compression at a diamond anvil [11], (18) the parameters of Jupiter's atmosphere [40], and (19) the adiabatic curve for the shock compression of hydrogen [34].

80% of the elements of the periodic table, critical temperatures and pressures are extremely high and are inaccessible to methods of static experiments. On the basis of their recent experiment, DeSilva and Katsouras [9], who were able to reach supercritical pressures via a fast electric explosion of metallic conductors, pointed out that solid-state metals lose their metallic conductivity upon a more significant expansion (by a factor of 5 to 7).

A method that employs the adiabatic expansion of matter preliminarily compressed by strong shock waves to pressures of the megabar range makes it possible to explore a wide region of the phase diagram of metals, including the vicinity of the phase-transition point [3, 10]. Measurements of thermodynamic (Cu, Pb, Bi, Fe, U) and radiative (Bi) properties of some metals according to this procedure permitted determining the equation of state, the coefficient of absorption, and the parameters of the critical points for the metals under study, but they did not confirm the hypothesis [4] that there occur plasma phase transitions caused by the dielectrization of metals in the supercritical region.

A considerable number of studies (see [11] and references therein) motivated by searches for metallic

hydrogen [11–13] in connection with its possible high-temperature superconductivity in a metastable medium [14] have been devoted to the metallization ($T = 0$) of dielectrics at high pressures. Estimates of the metallization pressure P^* that were obtained for various substances by methods of the band theory of solids fall within the megabar [$P^*(\text{H}_2) \approx 3$ Mbar [11–16], $P^*(\text{Xe}) \approx 1.5$ Mbar [17]) and ultramegabar [$P^*(\text{He}) \approx 110$ Mbar [18], $P^*(\text{Ne}) \approx 1.34$ Gbar [19]] ranges. Although the static experimental technique of diamond anvils presently enables one to obtain pressures as high as about 5 Mbar [11], only in recent years has it become possible to record the metallization of xenon at $P^* = 1.5$ Mbar [20] in such experiments; at the same time, hydrogen seems to remain a dielectric at $P \approx 3$ Mbar [11].

By using the technique of strong shock waves to ensure a compression and an irreversible heating of matter, one can obtain much higher pressures (the world record is about 4 Gbar [21]), the upper limit on them being constrained only by the intensity of the source of their generation and not by the strength of diamond under static conditions. Concurrently, the viscous dissipation of the kinetic energy of the flux in the shock-wave front, along with compression, leads to a considerable heating of matter, and this stimulates the

thermal ($k_B T \sim I$) ionization of a plasma, whose kinetics and thermodynamics have been studied in detail both for an ideal and for a strongly nonideal case (see [1] and [2, 3], respectively). In such experiments, the influence of density effects on the ionization equilibrium is not pronounced against the background of fully developed thermal ionization and is described by various models of ionization-potential reduction [1–3, 22]. It should be noted that a number of theoretical models lose thermodynamic stability upon extrapolation to the region of strong nonideality and that this is attributed in [4, 6, 22–25] to the occurrence of a first-order plasma phase-transition. Thermodynamic states realized to date in static and dynamic experiments [26–36] are displayed in the phase diagram of molecular hydrogen (H_2) in Fig. 1. Also given in the same figure are theoretical estimates for plasma phase transitions, along with relevant critical points [23, 24, 37–39].

In order to separate density and thermal effects of ionization, one must naturally try to suppress the effects of irreversible heating ($k_B T \ll I$) by implementing a quasi-isentropic compression. For this purpose, the compression of the substance in this study was accomplished by means of a sequence of direct and reflected shock waves that emerge upon their reverberation in planar and cylindrical geometries. For the source of generation, we employed explosive devices of end-face and cylindrical throwing. By using processes of multiple shock compression, it proves possible to implement an order of magnitude reduced heating and an approximately tenfold increased compression of a plasma in relation to what we have in a direct wave, as well as to record, in experiments with H_2 , He, and Xe, a five orders of magnitude increase in the plasma conductivity over a narrow density range peculiar to the regime of cold ionization of a plasma.

2. GENERATION AND DIAGNOSTICS

A typical layout of experiments to implement multiple shock compression of condensed hydrogen and inert gases in planar geometry is shown in Fig. 2 [36, 41, 42].

Shock waves were generated by the impact of a steel impactor (2) 1–3 mm thick and 30–40 mm in diameter accelerated by detonation products of a condensed high explosive (hexogen) (1) to velocities of 3–8 km/s with the aid of the gradient-cumulation effect [43]. Explosive throwing devices developed for these experiments ensured that, at the instant of impact against the bottom of the experimental assembly, the diameter of the flat part of the impactor was 15–30 mm. The absence of melting and evaporation of a shock-worker material, as well as the absence of mechanical fracture of the impactor during dynamic acceleration, was tested in a dedicated series of methodological experiments. The transition of a shock wave from a metallic screen (3) of thickness 1–1.5 mm to the substance under study (4)

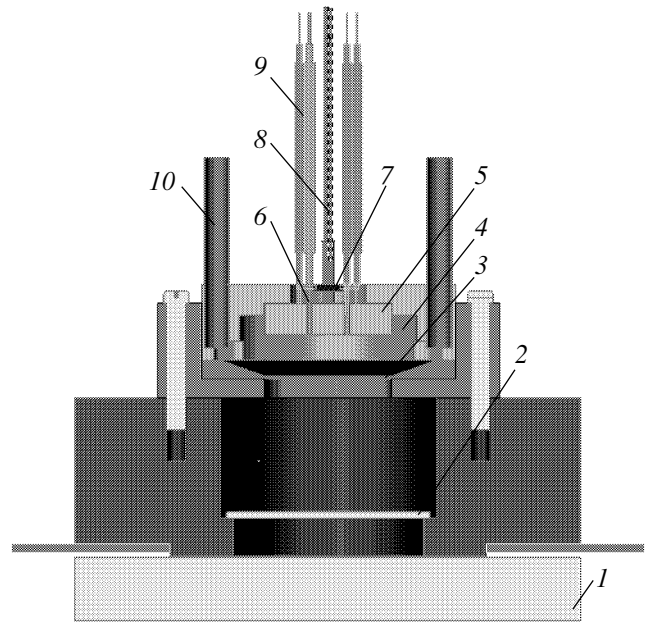


Fig. 2. Layout of experiments aimed at implementing multiple shock compression of condensed hydrogen and inert gases in planar geometry: (1) high-explosive charge, (2) steel plate, (3) bottom of the experimental assembly; (4) substance under study, (5) leucosapphire window, (6) indium electrodes, (7) shunting resistance, (8) quartz-quartz light guide, (9) coaxial electric cables, and (10) gas-supplying pipes.

having an initial thickness of 1 to 5 mm generated, in it, the first shock wave of amplitude pressure $P_1 = 0.02$ –0.8 Mbar; upon being reflected from a transparent sapphire window (5) 4–5 mm thick and 20 mm in diameter, this wave excited a repeated-compression shock wave. A further rereflection of shock waves between screen 3 and window 5 led to multiple shock compression of the sample to maximum pressures of $P \approx 1$ –2 Mbar, level of which was determined by the velocity of the impinging impactor, its thickness, and the dimensions of the substance being studied.

The initial states of the explored substances for a further multiple compression were either in the gas region of the phase diagram at pressure and temperature values of $P_0 = 5$ –35 MPa and $T_0 = 77.4$ –300 K, respectively, or in its liquid region at $P_0 \approx 0.1$ –1 MPa and $T \approx 20.4$ –160 K. In the latter case, liquefaction was performed from high-purity gases supplied to the assembly through pipes (10). In liquefying hydrogen, use was made of a two-contour system of cooling, the external contour being filled with nitrogen, while, in liquefying xenon, the internal contour of the cooling system was filled with ethanol. The temperature in the assembly was monitored by thermocouples and platinum resistance thermometers.

The process of multiple compression was observed by means of fast optic-electronic convertors, as well as by means of a five-channel fiber-optic-coupled pyro-

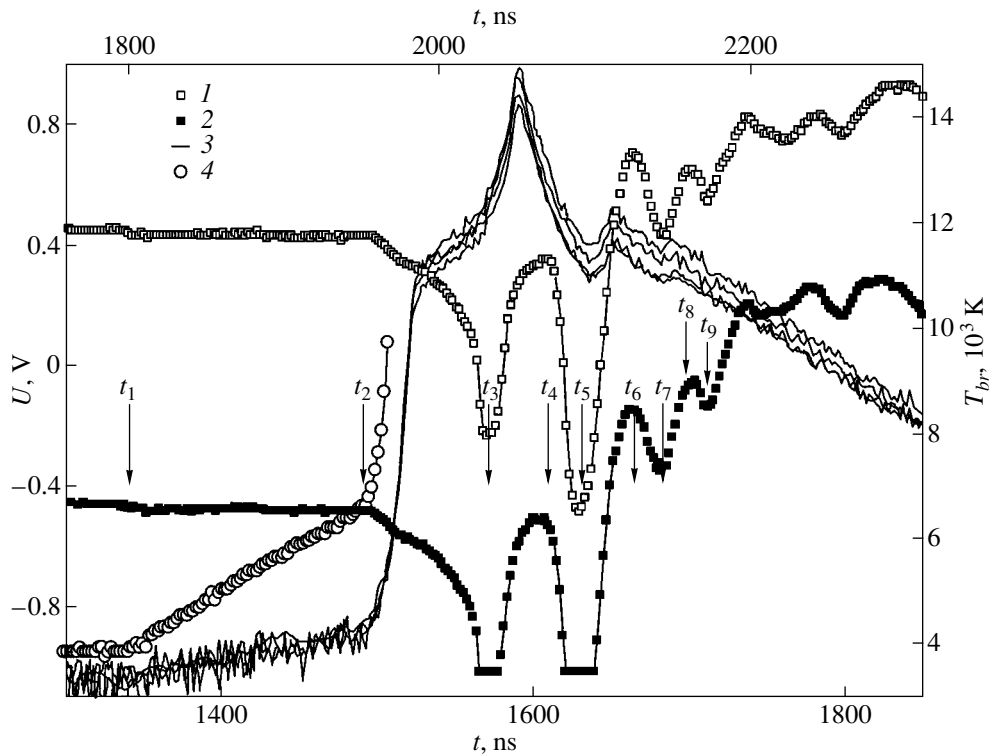


Fig. 3. Typical oscillogram of the experiment: (1, 2) voltage at the “positive” and the “negative” electrode and (3, 4) brightness temperatures of two channels for recording optical radiation (in this representation, the fourth temperature axis is linear in the range 3000–7000 K).

meter with time resolution of 2–5 ns (8). Since the shock-compressed sapphire of optic window 5 retained transparency up to $P \approx 20$ GPa and made it possible to record the instants of reflection of shock waves from its surface at still higher pressures and since its electric insulating properties were at an acceptable level under the conditions of compression up to pressures of about 2.2 Mbar [44], five to six reverberations of shock waves could be detected by measuring the conductivity of the compressed layer and optical radiation. Initial stages of the compression process (up to 20 GPa) were recorded in individual experiments with the aid of a VIZAR differential laser interferometer [45]. In order to synchronize the system for measuring the resistance of the compressed layer with that for detecting optical radiation, the light pulse from a laser diode that was connected before each experimental run through a light guide and through the convertor, along electric cables (9) of the system for measuring resistance.

In the scheme chosen for the present experiments (see [38, 41, 42]), the compression and irreversible heating of the substance under study were implemented by series of shock waves arising upon successive reflections from the sapphire window and the steel screen. A hydrodynamic analysis of the process revealed that, following the propagation of the first two waves through the compressed layer, a further compression proceeded

in a quasi-isentropic way. This made it possible to advance to the region of higher densities ($\rho/\rho_0 \sim 10$ –100) in relation to the case of single wave compression and to reduce the final temperature, whereby one enhances interparticle-interaction effects, which are of interest for the present investigation. The reverberation of shock waves manifests itself as distinct steps in the oscillograms of radiation and electrical conductivity (Fig. 3).

The measured instants of shock-wave arrival at the plasma-volume boundaries ($t_1 - t_9$) enable one to independently determine, by using the laws of mass, momentum, and energy conservation, the thermodynamic shock-compression parameters P , ρ , and E [3]. Data obtained in this way for the caloric and thermal equations of state of hydrogen, as well as of helium, which was chosen as a reference substance, up to pressures of 30–60 GPa are in accordance with the “chemical” non-ideal-plasma model [2, 3, 22] and with the solutions from the semiempirical equation of state of hydrogen [27, 46]. At pressures in excess of 60 GPa, however, no reliable information about the thermodynamics of the substances being studied could be obtained by means of the procedures used. In that case, the thermodynamic parameters of multiple shock compression at the final stage were calculated on the basis one-dimensional hydrodynamic codes that employ the

semiempirical equations of state from [27, 46] and [47] for hydrogen and structural materials, respectively.

This set of gasdynamic and temperature measurements was used to determine the thermodynamic parameters of shock compression at its initial stages; the results were also used as input data (along with the velocity W of the impinging impactor) in testing one- and two-dimensional gasdynamic codes according to which the parameters in question were determined for the case of higher pressures, densities, and temperatures of multiply compressed matter—the semiempirical equations of state [27, 46], valid over a wide region, were invoked in this determination. The errors in the P , ρ , and T values found in this way are 5, 10, and 20%, respectively.

The electrical conductivity of a shock-compressed plasma was determined by a probe method. An electric current was supplied to the shock-compressed plasma under study by means of electrodes (6) that were arranged orthogonally to the plane of the shock-wave front. Further, the current propagated along the shock-compressed sample and then arrived at the surface of steel screen 3, whereupon it left the compressed region through a grounding electrode. The arising electric signals transferred by high-frequency coaxial cables (9) were recorded by multichannel digital oscilloscopes whose transmission bandwidth was 500 MHz. Use was made of two- or three-electrode schemes for recording resistance. In the second case, whose circuit diagram is given in Fig. 4, we were able to get rid of cophasal noises and to record the instants of wave reflection not only from the optic window but also from the screen.

The instants t_1, t_3, t_5, t_7 , and t_9 corresponded to wave reflection from the window, and this was recorded with the aid of an electric (lines 1, 2 in Fig. 3) and an optical (lines 3, 4) in Fig. 3) procedure; the instants t_2, t_4, t_6 , and t_8 corresponded to wave reflection from the screen. With the aim of eliminating breakdown and arc effects in transmitting the transport current through a plasma, its density was maintained at a level not exceeding 10^4 A/cm². By varying this quantity within the range 10^3 – 10^4 A/cm² in a dedicated series of measurements, it was shown that the current–voltage characteristic of the plasma is linear. Determination of the plasma electrical conductivity on the basis of the plasma-gap resistance measured in this way was performed by resorting to numerical and electrostatic simulations of the corresponding electrostatic problem. As a result, the accuracy in measuring the plasma electrical conductivity was estimated at 20 to 50%.

The second series of measurements was performed by employing shock compression under the conditions of cylindrical geometry [48–50] (see Fig. 5).

A cylindrical charge of a high explosive (an alloy formed by trotyl and hexogen in a ratio of 40 : 60), its outer diameter being 30 cm, was initiated over the outer surface at 640 points that generated, at the inner surface of the charge, a highly symmetric detonation wave (the

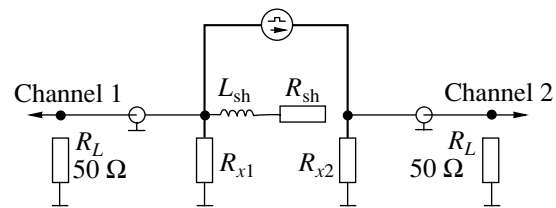


Fig. 4. Circuit diagram of the measurements.

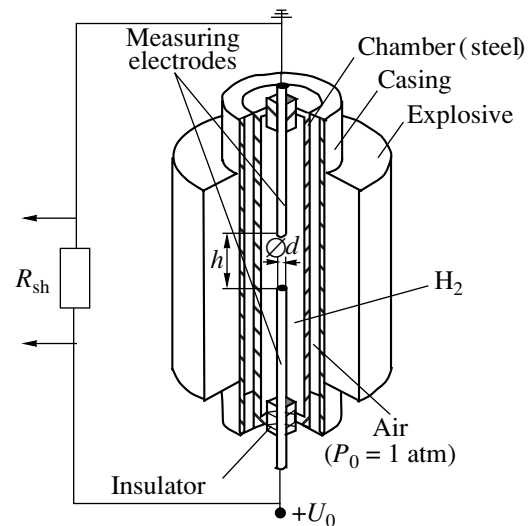


Fig. 5. Layout of cylindrical compression.

difference in time of arrival was not greater than 100 ns). The arrival of this wave at the inner surface caused the centripetal motion of the steel impactor at an initial velocity of $W \approx 5$ km/s. The deceleration of this cylindrical impactor against the metallic surface of the chamber filled with the gas under study at an initial pressure of up to 70 MPa generated a converging shock wave, whose intensity increased as it traveled to the center, this increase being governed by the regularities of geometric cumulation [51]. Thereafter, there occurred successive reflections of the shock wave from the center of symmetry and from the moving inner surface of the chamber, and this gave rise to multiple shock compression, which, as in the case of planar geometry, proved to be close to isentropic compression.

At each instant of time, the profiles of thermodynamic parameters of multiple compression were determined on the basis one- or two-dimensional gasdynamic calculations employing, for the high explosive, the structural materials of the assembly, and target plasmas, semiempirical equations of state that are valid over a wide region. In some special experiments, the process of cylindrical explosive compression was monitored by measuring the velocity of the impactor by electric-contact and fiber-light optical basis methods, as well as by means of examination along the axis with

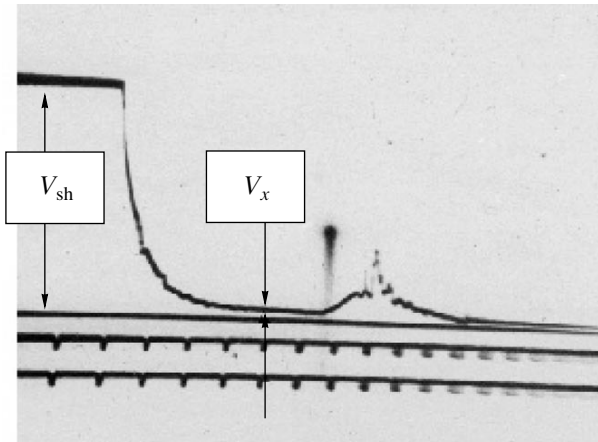


Fig. 6. Oscillogram of the experiment where the initial hydrogen pressure was 70 MPa (the time-scale division here is 1 μ s).

two hard-radiation sources [52] emitting beams crossed at an angle of 135°; this made it possible to follow the dynamics of compression and to test the quality of gas-dynamic calculations and yielded additional boundary conditions for the codes used in those calculations. The parameters found in this way for the shock-compressed plasma in the device being considered had the following values: for deuterium, the pressure was 1.25–1.44 TPa at temperatures of 12500–14000 K and densities of 2–2.4 g/cm³; for xenon, the pressure and density were 200 GPa and 13 g/cm³, respectively, the latter value being nearly five times as great as the density of solid Al.

The electrical conductivity was measured according to the classic two-point circuit diagram [53] involving a reference resistance connected in parallel with the resistance of the sample under study. The resistance of hydrogen was determined with the aid of two stainless-steel electrodes 2 mm in diameter arranged on the axis of the device with a gap length of $h = 6.5$ mm between their end faces. This procedure of measurements employed the discharge of a large-capacitance capacitor through the resistance R_{sh} shunting the hydrogen

sample. The decrease in the compressed-hydrogen resistance R_x led to a decrease in the total resistance, with the result that the voltage across the measuring electrodes changed, which was recorded by an oscilloscope. In these experiments, R_{sh} was 3 Ω . Figure 6 displays an oscillogram that was obtained in one of the experiments at an initial hydrogen pressure of $P_0 = 70$ MPa. The resistance estimated by using this oscillogram is $R_x \approx 0.2 \Omega$.

In determining the electrical conductivity on the basis of the measured resistance values, the actual geometry of the current distribution between the electrodes was taken into account, along with the geometry of the electrodes at each specific instant of compression and with the results obtained by calculating, according to hydrodynamic codes, the profiles of the thermodynamic parameters of hydrogen. The error in the electrical-conductivity values found in this way was estimated at 50%.

The characteristic plasma parameters obtained in some experiments are quoted in Table 1.

3. EXPERIMENTAL RESULTS FOR THE ELECTRICAL CONDUCTIVITY; MODEL OF PRESSURE-PRODUCED IONIZATION

Experiments aimed at implementing multiple shock compression of hydrogen and inert gases make it possible to obtain physical information about an as-yet-unexplored part of the phase diagram, which is depicted in Fig. 1 for hydrogen. One can see that the region of pressures of up to 15 Mbar and temperatures of 3000 to 7000 K was reached by means of dynamic compression. Concurrently, densities are realized that are one order of magnitude higher than those of solid hydrogen and solid inert gases under normal conditions, in which case the mean spacing between protons, $n^{-1/3} \sim 1$ Å, is commensurate to the typical sizes of both molecules (about 0.74 Å) and atoms in the ground state.

From the point of view of physics, this region is of interest since this is the region of strong interaction

Table 1

Substance	Initial state	Final state	P , GPa	ρ , g/cm ³	T , 10 ³ K	σ , (Ω cm) ⁻¹
Planar geometry						
H ₂	$P_0 = 25.6$ MPa, $T_0 = 77.4$ K	Maximum compression	227	0.94	5.3	1600
He	$P_0 = 28$ MPa, $T_0 = 77.4$ K	Maximum compression	126	1.37	15	1080
Xe	$P_0 = 0.1$ MPa, $T_0 = 160$ K	Maximum compression	126	10	25	500
Cylindrical compression						
H ₂	$P_0 = 50$ MPa, $T_0 = 293$ K	Maximum compression	1440	2.4	14	550
	$P_0 = 70$ MPa, $T_0 = 293$ K	Maximum compression	1250	2	12.5	1100

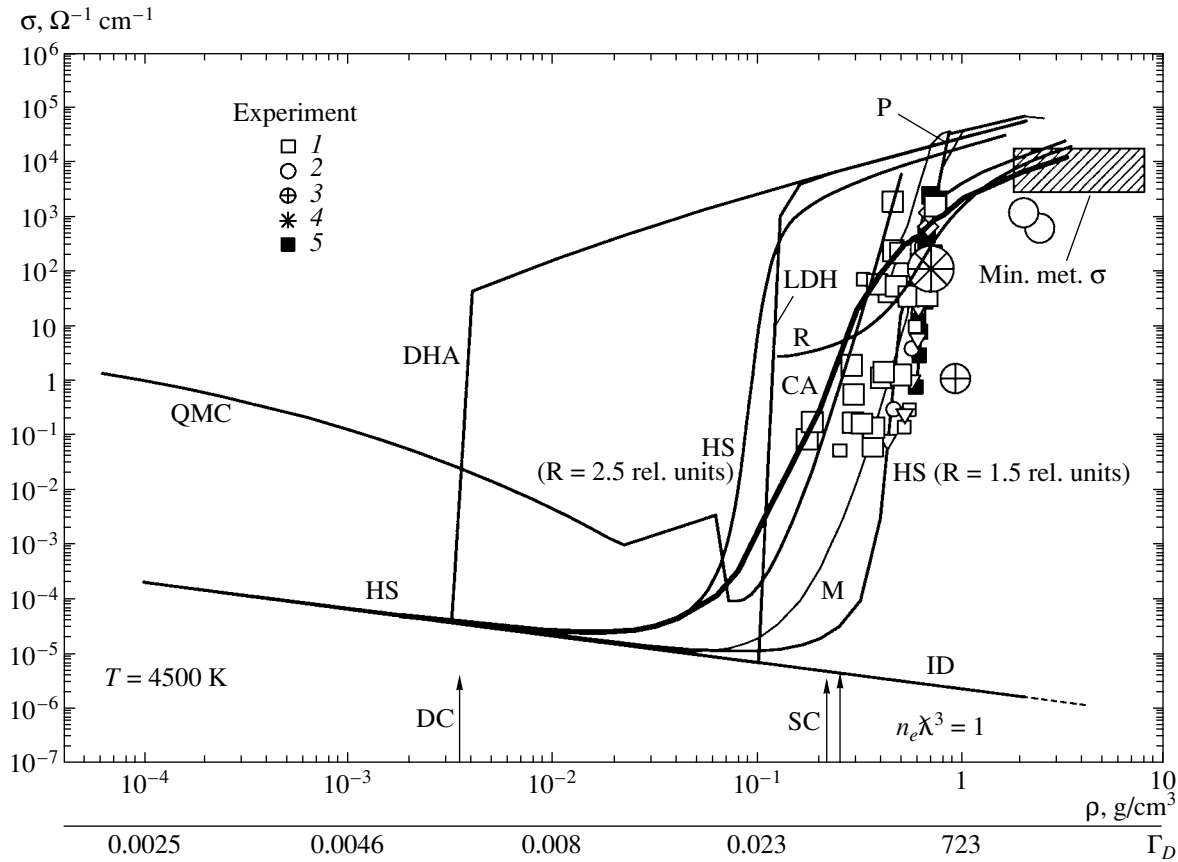


Fig. 7. Electrical conductivity of hydrogen as a function of density. The experimental data of the present study were obtained for (1) planar systems and (2) cylindrical systems. The remaining data were borrowed from (3) [29] and (4) [30] (magnetic compression) and from (5) [35] (experiments with light-gas guns).

concerning both interatomic (intermolecular) interaction ($\Gamma_a = r_a n_a^{-1/3} \sim 1$ —that is, r_a , which is the molecular or the atomic size, is commensurate with the interparticle spacing $n_a^{-1/3}$) and, the latter implying that the mean interaction energy of charged particles,

$$E_C = e^2/r_D, \quad r_D = \left(4\pi e^2 \sum_i Z_i^2 n_i / k_A T \right)^{1/2},$$

is much greater than the mean kinetic energy of thermal motion, E_T ($\Gamma_D = E_C/E_T \sim 10$). The situation is additionally complicated by the fact that the type of statistics changes upon compression—electrons become degenerate, $n_e \chi_e^3 \approx 200$ [$\chi_e = (2\pi\hbar^2/m_e k_B T)^{1/2}$ is the thermal de Broglie wavelength], with the result that $E_T \sim k_B T$ as the scale of the kinetic energy of particles gives way to the Fermi energy,

$$E_F = \frac{(3\pi^2 n_e)^{2/3}}{2m_e}, \quad E_T \sim E_F.$$

All these circumstances greatly complicate theoretical description of strongly nonideal states [2, 3], hindering the application of perturbation theory and of parameter-free computer Monte Carlo and molecular-dynamics methods in their classic formulation [54], which were developed for Boltzmann statistics.

Our experimental results for the electrical conductivity of shock-compressed hydrogen and inert gases are displayed in Figs. 7–11, along with the results obtained on the basis of some theoretical models [1–3, 22, 37, 24, 55, 56] and the results of other measurements [29, 30, 35, 36, 41, 42, 57–65].

Let us first point out some general features in the behavior of the electrical conductivity of a strongly nonideal plasma. The most prominent feature is that, at final stages of compression, the electrical conductivity of the plasma increases sharply (by three to five orders of magnitude) in the process of compression in a nar-

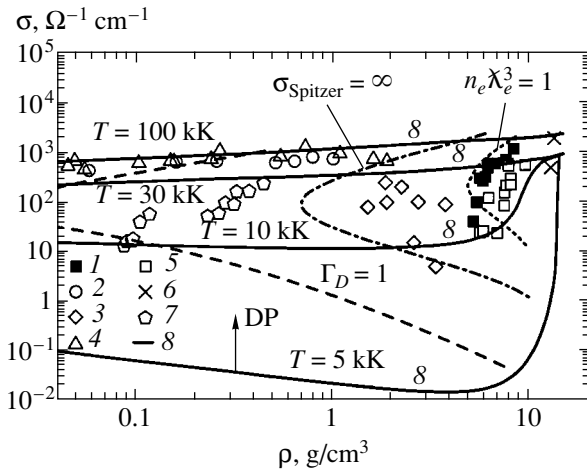


Fig. 8. Electrical conductivity of xenon as a function of density. The displayed experimental data were borrowed from (1) [49], (2) [57], (3) [58], (4) [59], (5) [41], (6) [60], and (7) [61]. Also plotted in this figure are the electron-degeneracy line ($n_e \lambda_e^3 = 1$), the line on which the parameter of Coulomb nonideality takes the constant value of $\Gamma_D = 1$, and the line on which the electrical conductivity calculated by Spitzer's formula goes to infinity ($\sigma_{\text{Spitzer}} = \infty$). Solid lines 8 represent the electrical conductivity calculated on the basis of the model formulated in the main body of the text.

row range of “compressed” densities ($\rho \approx 0.3\text{--}1\text{ g/cm}^3$ for hydrogen, and $\rho \sim 8\text{--}10\text{ g/cm}^3$ for xenon) at megabar pressures, reaching values of about $10^2\text{--}10^3\text{ }\Omega^{-1}\text{ cm}^{-1}$, which are characteristic of alkali metals. Our measurements exhibit a pronounced threshold effect in density and are therefore in a qualitative contradiction with models of weakly nonideal plasma [1], which predict a monotonic decrease in the plasma electrical conductivity in response to its isothermal compression [1].

Indeed, it is well known that, at low degrees of the ionization of a plasma,

$$\alpha_i = \frac{n_e}{n_a + n_e} \ll 1,$$

its electrical conductivity is determined by the scattering of electrons on neutral particles and is qualitatively described by the Lorentz formula [3], according to which the electrical conductivity is in direct proportion to the concentration of free electrons; that is,

$$\sigma_{ea} = \frac{2\sqrt{2}}{3\sqrt{\pi}} \frac{e^2}{m_e^{1/2} (k_B T)^{1/2}} \frac{n_e}{n_a q_{ea}^*(T)}, \quad (3.1)$$

where q_{ea}^* is the averaged cross section for electron scattering by atoms:

$$\frac{1}{q_{ea}^*(T)} = \frac{1}{(k_B T)^2} \int \exp\left(-\frac{E}{k_B T}\right) \frac{dE}{q_{ea}(E)}.$$

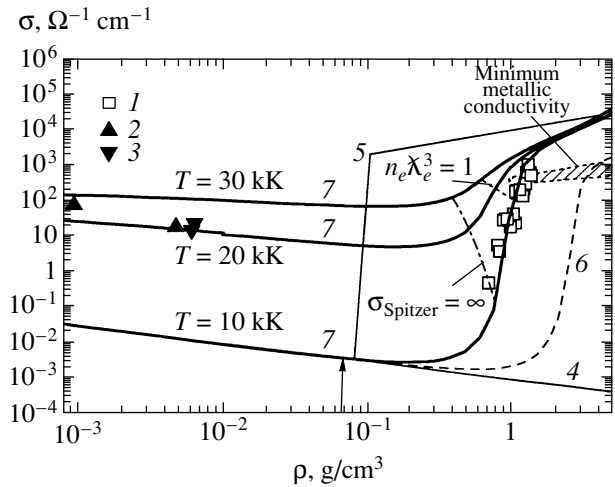


Fig. 9. Electrical conductivity of helium as a function of density: (1), (2), and (3) experimental data from [42], [57], and [61], respectively; (4) electrical conductivity calculated with the plasma composition corresponding to the model of an ideal plasma; (5) results obtained with the plasma composition calculated on the basis of the Debye–Hückel model [1]; (6) results obtained with the plasma composition calculated on the basis of the bounded-atom model [2, 22] featuring a fixed radius of the helium atom ($r_a = 1.3a_0$); and (7) results of the present study.

In turn, the composition of a plasma is described by Saha's ionization-equilibrium equation [2]

$$\frac{n_e n_i}{n_a} = \frac{2Q_i}{Q_a} \chi_e^{-3} \exp\left[-\frac{I - \Delta I(n_e, n_0, T)}{k_B T}\right], \quad (3.2)$$

where Q_a and Q_i are the partition functions for atoms and ions, respectively, I is the ionization potential, and

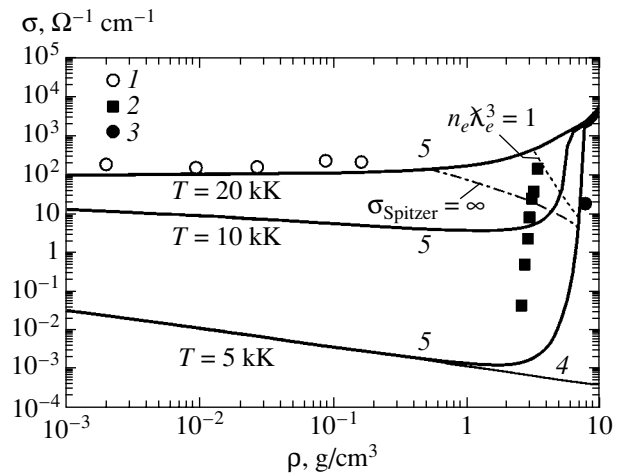


Fig. 10. Electrical conductivity of argon as function of density: (1), (2), and (3) experimental data from [57], [62], and [63], respectively; (4) electrical conductivity calculated with the plasma composition corresponding to the model of an ideal plasma; and (5) results of the present study.

ΔI is the reduction of the ionization potential due to interparticle interaction (nonideality). Thus, one can see that, at $\alpha_i \ll 1$, it follows from Eqs. (3.1) and (3.2) that, in the absence of interaction ($\Delta I = 0$, and $Q_i, Q_a = \text{const}$), the electrical conductivity under the conditions of isothermal compression is given by

$$\sigma \sim \alpha_i \sim 1/\rho,$$

which corresponds to the curves for an ideal plasma in Figs. 7, 9, and 10.

Nonideality, which must be included under the present conditions for determining the composition of a plasma, is taken into account here by introducing a density-dependent quantity ΔI and less significant dependences for Q_i and Q_a , whereby one arrives at a nonthermal growth of the degree of ionization and at an increase in the plasma electrical conductivity upon isothermal compression in accordance with Eq. (3.1). On the curve representing the electrical conductivity as a function of density at $T = \text{constant}$, there appears a minimum, its depth being greater for lower temperatures. With increasing temperature, this minimum levels out as soon as thermal-ionization effects (at $k_B T \sim I$) become more pronounced than effects associated with pressure-produced ionization, which are significant at $k_B T \ll I$.

As the density increases further at a given temperature, ionization processes described by relation (3.2) are completed. Thereupon, one deals with a strongly ionized ($\alpha_i \sim 1$) weakly nonideal plasma, where, instead of Eq. (3.1), it is necessary to use the Spitzer approximation (which is valid in the case of a nondegenerate plasma) [3]

$$\sigma_{ei} = \gamma(Z) \frac{4\sqrt{2}(k_B T)^{3/2}}{\pi^{3/2} Z e^2 m_e} \frac{1}{\Lambda} \quad (3.3)$$

or, in the case of Fermi statistics, the relation

$$\sigma \sim \frac{n_e}{\Lambda}, \quad (3.4)$$

where Λ is the Coulomb logarithm. This means that, at high temperatures, the exponential dependence in (3.1) and (3.2) gives way to a weaker [logarithmic in the case of (3.3) or linear in the case of (3.4)] dependence on the carrier concentration. In this case, we can take, for an estimate of conductivity, the so-called Regel–Ioffe “minimal metal” conductivity, which is widely used in the theory of simple metals and semiconductors; that is,

$$\sigma \sim \frac{n_e R_S}{v_T}, \quad (3.5)$$

where R_S is the radius of the Wigner–Seitz cell and v_T is the mean thermal velocity of electrons.

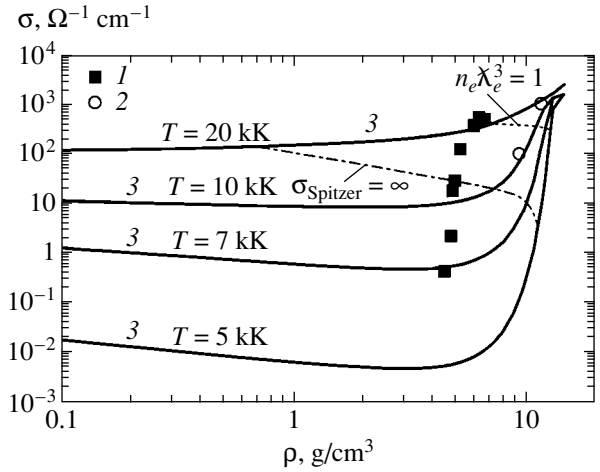


Fig. 11. Electrical conductivity of krypton as function of density: (1) and (2) experimental data from [64] and [65], respectively, and (3) results of the present study.

We can see that the exponential growth of the number of carriers due to the reduction of the ionization potential because of strong interparticle interaction in plasmas of condensed densities is the main reason behind the sharp increase in the measured electrical conductivity.

It should be emphasized that, in exactly the same way as the semiconductor thermal-excitation model (see, for example, [66]) featuring an energy gap $\Delta(\rho)$ that decreases with increasing density, the plasma pressure-produced-ionization model that is based on Eqs. (3.1) and (3.2), which is discussed here, leads to an exponential variation of the electrical conductivity with temperature:

$$\sigma \sim \sigma_0 \exp(-\Delta(\rho)/k_B T).$$

This model was used in [35] to analyze experiments with light-gas guns.

Thus, the data obtained here for the electrical conductivity at $k_B T \ll I$ provide a unique possibility for adequately choosing thermodynamic models that would describe the reduction of the ionization potential. For example, an analysis of the data in Figs. 7–11 reveals that the standard Debye–Hückel model (DHA curve in Fig. 7 and curve 5 in Fig. 9) strongly overestimates effects of Coulomb interaction, leading to pressure-produced ionization at densities that are two orders of magnitude lower than their experimental counterparts.

Having performed the above qualitative analysis, we will now perform quantitative calculations of physical parameters that characterize a dense plasma and compare the results obtained in this way with experimental data.

4. THERMODYNAMICS OF MEGABAR-RANGE PLASMAS

As a model intended for describing experiments devoted to the shock and quasi-isentropic compression of plasmas, we consider the bounded-atom model [67], which explicitly takes into account the finiteness of the phase space for the realization of the bound states of atoms and ions and which was previously used in [2, 3,

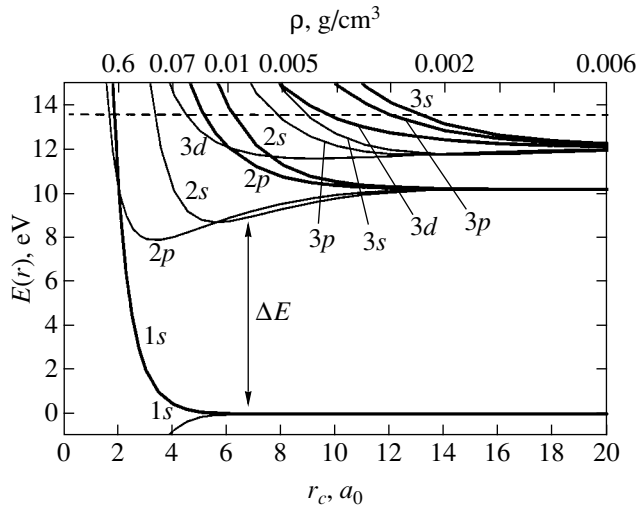


Fig. 12. Energy spectrum of the hydrogen atom for (thick curves) $f_{nl}(r_c) = 0$ and (thin curves) $f'_{nl}(r_c) = 0$.

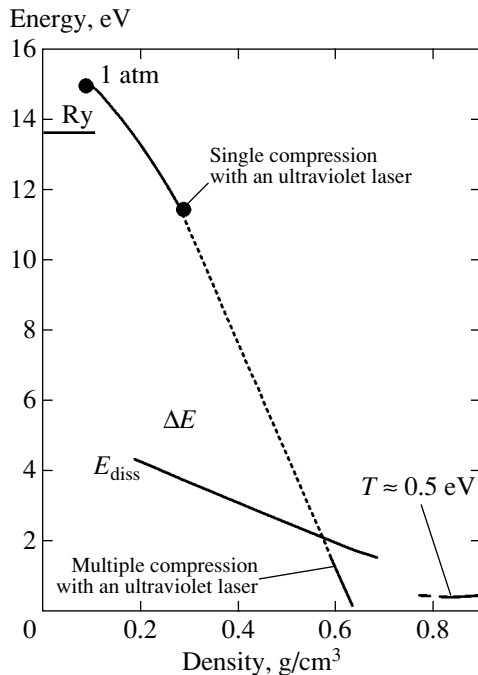


Fig. 13. Bandgap of deuterium.

67] to describe the thermodynamics of shock-compressed inert gases and cesium. As a matter of fact, this model is a generalization of the Wigner–Seitz solid-state model [1, 3] to the region of condensed-density plasmas via the inclusion of thermal and density-ionization effects. Within this model, atoms and ions are treated as rigid spheres, whose thermodynamic functions are constructed on the basis of molecular-dynamics and Monte Carlo calculations, the contribution of the bound electrons of these atoms and ions being described in the quantum-mechanical Hartree–Fock approximation. Figure 12 shows the energy spectrum of a compressed hydrogen atom.

In the calculation of this spectrum, the radial component of the wave function was required to satisfy the boundary conditions

$$f_{nl}(r)|_{r=r_c} = 0, \quad \frac{\partial f_{nl}(r)}{\partial r} \Big|_{r=r_c} = 0.$$

Within the solid-state model [68], this corresponds to the upper and lower boundaries of the energy band within which the relevant energy level of an isolated ($r_c \rightarrow \infty$) atom occurs as the result of compression (decrease in r_c). In this approach, the width of the forbidden band, ΔE (energy gap), can be taken as the energy difference between upper boundary of the ground-state band (curve $1s$) and the lower boundary of the band built on the first excited stated (curve $2p$); as can be seen from Fig. 13, the energy gap, which decreases with increasing density, is in accordance with the experimental data reported in [44, 69] and obtained from a direct treatment of data from experiments devoted to multiple compression of hydrogen and deuterium. Versions of this model were successfully used to describe the thermodynamics of metal plasmas in the region of high and ultrahigh (up to 4 Gbar) pressures [70–72].

The parameter region investigated in the experiments being discussed is characterized by extremely complicated and diversified processes that must be reflected in the corresponding physical models. It should be noted first of all that, in the course of compression, the thermodynamic plasma composition may change sharply, which is accompanied by the emergence of strong interparticle interactions, including Coulomb interaction (between electrons and ions), polarization interaction (between charged and neutral particles), and short-range interaction (between neutral particles). Since the typical interparticle spacing in the plasmas considered here is commensurate with characteristic sizes of atoms and ions, the phase-space part occupied by them becomes inaccessible to other particles; as a result, their kinetic energy grows, and so do the corresponding contributions to the free energy of such strongly compressed disordered structures. Moreover, the energy spectrum of bound states undergoes changes in atomic and molecular systems subjected to

a strong compression. Also, it is necessary to take into account the change in statistics (from Boltzmann to Fermi statistics) for continuous-spectrum electrons, since, under the conditions being considered, the degeneracy parameter $n_e \chi_e^3$ changes from 0.001 to 200.

In the present study, the following items of the full thermodynamic approximation were used in calculating the thermodynamic parameters of plasmas in the megabar range of pressures.

The free energy of a quasineutral mixture of electrons, ions, atoms and molecules can be broken down into the contribution of the ideal-gas component and the term that takes into account interparticle interaction; that is,

$$F \equiv F_i^0 + F_e^0 + F_{ii,ie,ee,\dots}^{\text{int}}. \quad (4.1)$$

It is assumed that heavy particles (atoms, ions, molecules) obey Boltzmann statistics, their contribution having the standard form

$$F_i^0 = \sum_j N_j k_B T \left(\ln \frac{n_j \chi_j^3}{Q_j} - 1 \right), \quad (4.2)$$

where Q_j stands for the partition functions of atoms and ions.

(A) **Electron degeneracy.** Electrons are treated as a partly degenerate ideal Fermi gas:

$$F_e^0 = 2V k_B T \pi^{-1/2} \chi_e^{-3} \times \left[(\mu_e/k_B T) I_{1/2}(\mu_e/k_B T) - \frac{2}{3} I_{3/2}(\mu_e/k_B T) \right], \quad (4.3)$$

$$\frac{P_e^0}{n_e k_B T} = \frac{2 I_{3/2}(\mu_e/k_B T)}{3 I_{1/2}(\mu_e/k_B T)}. \quad (4.4)$$

Here, the electron density n_e and the chemical potential μ_e are related by the equation

$$n_e \chi_e^3 = 2\pi^{-1/2} I_{1/2}(\mu_e/k_B T), \quad (4.5)$$

$$I_t(x) = \int_0^\infty \frac{y^t dy}{1 + \exp(y - t)}.$$

The inclusion of electron-degeneracy effects is of paramount importance in the phase-diagram region discussed here, since the degeneracy parameter $n_e \chi_e^3$ can be much greater than unity in this region.

(B) **Coulomb interaction.** We applied a version of the pseudopotential-model for multiple ionization [73, 74]. The inclusion of the fact that, at short distances, the interaction of free charges deviates from a Coulomb

form is a key point of this model, and there arises, upon explicitly taking this deviation into account, a noticeable positive shift not only in the potential energy of free charges but also in their mean kinetic energy. It should be noted that the depth of the electron-ion pseudopotential, $\Phi_{ie}^*(0)$, is related, in the model, to the boundary separating, in the partition function (4.2), free states of each electron-ion pair from bound states. The electron-ion pseudopotential in the Glauber-Yukhnovskii form is given by (Fig. 14)

$$\Phi_{ie}^*(r) = -\frac{Z_i e^2}{r} (1 - e^{-r/\sigma_{ie}}), \quad \sigma_{ie} \equiv \sigma_{ie}(n, T), \quad (4.6)$$

$$\Phi_{\alpha\alpha}^*(r) = \frac{Z_\alpha Z_\alpha e^2}{r}, \quad \alpha = i, e.$$

For potential (4.6), the parameters of correlation functions were determined from conditions that are formulated immediately below and which are quite general and are valid at arbitrary values of the Coulomb nonideality parameter

$$\Gamma_D = [4\pi(e^2/k_B T) \sum n_\alpha z_\alpha^2]^{-1/2}.$$

Specifically, these are

(i) the condition of local electroneutrality,

$$\int \left\{ n_{ei} [F_{ei}(r) - 1] + \sum_j n_{ij} Z_j [F_{ij}(r) - 1] \right\} d\mathbf{r} = -Z_i; \quad (4.7)$$

(ii) the condition of dipole screening,

$$\int \left\{ n_{ei} [F_{ei}(r) - 1] + \sum_j n_{ij} Z_j [F_{ij}(r) - 1] \right\} \times \left(\frac{r}{r_D} \right)^2 d\mathbf{r} = -3Z_i; \quad (4.8)$$

(iii) the nonnegativity of correlation functions,

$$F_{ik}(r) \geq 0; \quad (4.9)$$

(iv) the relation between the screening-cloud amplitude and the depth of the electron-ion pseudopotential,

$$F_{ei}(0) \equiv 1 + \Psi_{ei}(0) \approx \beta \Phi_{ei}^*(0), \quad F_{ii}(0) \approx 0. \quad (4.10)$$

At $\Gamma_D \ll 1$, corrections that are associated with the interaction of charges and which were obtained from the conditions in (4.6)–(4.10) are close to Debye corrections, while at $\Gamma_D \gg 1$, they are smaller.

(C) **Short-range repulsion.** The contribution of the short-range repulsion of molecules, atoms, and ions is

described phenomenologically within the soft-sphere approximation [75] generalized to the case of a multi-component mixture; that is,

$$\frac{\Delta F_{ss}}{Nk_B T} = C_s y^{s/3} (\epsilon_{ss}/k_B T) + \frac{s+4}{6} Q y^{s/9} (\epsilon_{ss}/k_B T)^{1/3}, \quad (4.11)$$

$$y = \frac{3Y\sqrt{2}}{\pi}, \quad Y = \frac{4\pi r_c^3}{3} = \frac{\pi\sigma_c^3}{6}, \quad r_c = \left[\frac{\sum n_j r_j^3}{\sum n_j} \right]^{1/3},$$

where

$$C_s = 6 + \frac{6.669}{s-3} = 1.043(s-4)^{0.389} \exp[0.156(4-s)]$$

is the Madelung constant for the potential $V(r) = \epsilon(r/\sigma)^{-s}$.

We note that the corrections for short-range repulsion to the chemical potential,

$$\frac{\Delta \mu_{jss}}{k_B T} = \frac{\Delta F_{ss}}{Nk_B T} + \frac{\Delta P_{ss}}{nk_B T} \left[\frac{r_j}{r_c} \right]^3, \quad (4.12)$$

are different for particles having different radii, and this determines the decrease in the ionization (dissociation) energy with increasing matter density.

The above thermodynamic model provides a correct asymptotic behavior at low plasma densities, where it coincides with well-known theories of dilute plasma. In the region of extremely high densities, the applicability of this model was tested by comparing the results that it yields with available experimental data on the thermodynamics of the plasmas of alkali metals [2], inert gases [55–57], and shock-compressed strongly porous metals [72, 74]. Considered individually below are special features of the calculation for each element of interest.

4.1. Hydrogen

In the phase diagram of hydrogen (Fig. 1), the transition to the metallic state at low temperatures is shown in accordance with the estimates given in [22] at a pressure of about 300 GPa. The triple point at which the metal phase coexists with condensed molecular hydrogen and a molecular liquid is predicted in [22] to occur at $P = 100$ GPa and $T = 1500$ K. There are two critical points (CPs) in the molecular-liquid phase. One of these, CP_1 , and the curve along which a molecular gaseous hydrogen and a liquid coexist are well known to lie in the low-temperature region. The position of the second critical point (CP_2), which is of greatest interest to us, and the position of the coexistence curve (curve 12) that is associated with a sharp change in the degree of dissociation and ionization of hydrogen are not known precisely. According to the estimates presented in [22], $T[CP_2] = 16500$ K, $P[CP_2] = 22.8$ GPa, and

$\rho[CP_2] = 0.13$ g/cm³. Also shown in Fig. 1 are estimates of other authors [23, 24, 37–39] for the coexistence curve and for the critical point at which this plasma phase transition occurs (curves 12–16).

It can be seen that the parameter region corresponding to multiple shock compression in planar systems [36] (region 9) and in experiments with light-gas guns (LG) [34, 35] (curves 7, 8), as well as in cylindrical systems [26, 27] (curves 4, 5), partly overlap this rather large region of the possible existence of a plasma phase transition. The shock adiabatic curves of a single compression of liquid hydrogen (deuterium) that were obtained in experiments with high-power lasers [31, 32] (curves 10, 11), in a high-current Z pinch [33] (curve 3), and in explosive spherical systems [28] (star 6) also occur in the region of our interest, but they lie at higher temperatures. Temperatures of about 700 K were realized in experiments devoted to the isentropic compression of hydrogen by strong magnetic fields in explosive magnetic-compression systems [29, 30] (boxes 1, 2). Pressures of up to 300 GPa were obtained via the isothermal compression of hydrogen ($T \approx 300$ K) in diamond anvils (DA) [11] (curve 17). The region where strong Coulomb interaction is operative and the region where the degeneracy of the electron component is significant lie above the curves $\Gamma_D = 1$ and $n_e \lambda_e^3 = 1$, respectively. Curve 19 characterizes the behavior of the shock adiabatic curve for liquid hydrogen, while curve 18 represents parameters that are realized in Jupiter's atmosphere [40]. Figure 1 also displays the regions of typical parameters achievable with the aid of ordinary and explosive shock tubes (see [76] and [77], respectively), in discharges, and in usual low-current pinches [3].

As can be seen, the existence of a large “monomolecular” region ($\rho \leq 0.3$ g/cm³, $-\mu_H \geq D(H_2) \approx 4.5$ eV), where the thermodynamics of hydrogen is almost completely determined by H_2 – H_2 interaction, is a feature characteristic of hydrogen. Within the soft-sphere model [75], which is used in the present study, the parameters of the H_2 – H_2 interaction were chosen here to be maximally close to those recommended within the rigorous “nonempirical” atom–atom approximation [78], the noncentrality of this interaction being disregarded. The calculations have revealed that the use of the soft-core repulsion $V(r) \propto 1/r^6$ makes it possible to describe the molecular part of the $T = 0$ isotherm (“cold curve”) and a considerable part of shock-wave experiments, as well as the results of precise Monte Carlo calculations of $H_2 + H_2$ thermodynamics [78].

The main problem of the chemical model in describing nonideality, including nonideality in the case of dense hydrogen, is that of correctly specifying the entire set of potentials that would simulate the interactions between all members of the mixture being considered. This concerns the interactions involving both charged and neutral particles—first of all, interactions

in $\text{H}_2\text{-H}$ and H-H pairs. It is of importance that the effective interaction of free atoms that appears in the chemical model differs radically from the singlet (attractive) and triplet (repulsive) branches of the total potential of H-H interaction that are obtained from a rigorous theory, since the contribution of H-H pairs involved in the singlet-branch interaction has already been taken into account in the discharge of intramolecular motion. This is all the more justified for the effective interaction involving (free) charged particles, since, in the chemical model, the contributions of free and bound states must be consistent [see the approximation specified by Eqs. (4.6)–(4.10)]. At present, there is a serious discrepancy between the results obtained within different approaches for the form and parameters of these potentials. Off the monomolecular region, the most glaring contradictions are those in the parameters of the short-range repulsion in H-H and H-H_2 pairs. We note that, according to the present calculations, the parameters of the effective potentials of $\text{H}_2\text{-A}^\pm$ interactions (where the symbol A^\pm stands for all charged components) are of no lesser importance. For one of the versions, we would like to indicate the results obtained within the nonempirical atom-atom approximation [78], which lead to relatively large “intrinsic volumes” of the hydrogen atom. In terms of the soft-sphere-model modification introduced in [75] and used here, the results presented in [78] correspond almost exactly to the “additive-volume” approximation,

$$[d(\text{H}_2)]^3 \approx 2[d(\text{H})]^3.$$

For $\rho \leq \rho^* \approx 0.3 \text{ g/cm}^3$, this choice leads to results that agree, for $T \leq 10 \text{ kK}$, with the results of precise Monte Carlo calculations [78] and, for $T \geq 10 \text{ kK}$, with the nonanomalous part of the results obtained by means of a quantum Monte Carlo method (PIMC [79]). At such temperatures, the data are also in satisfactory agreement with the results produced by other versions of *ab initio* approaches, including the method of quantum molecular dynamics (TBMD [80]) and the method of wave packets (WPMD [81]).

Figure 15 displays the entire body of currently available experimental data on single shock compression of liquid deuterium.

Pressures of up to 25 GPa (point 1 in Fig. 15) were achieved in a direct shock wave generated in experiments with light-gas guns [34]. Investigations aimed at generating shock waves with the aid of high-power lasers [31, 32] (points 2, 3) made it possible to obtain pressures of up to 300 GPa and to discover an anomalously high compressibility of deuterium at a pressure of $P > 40 \text{ GPa}$. However, more recent results that emerged from the Z-pinch experiment reported in [33] (points 4) and from the experiment of Belov *et al.* [28] (points 5) with explosive spherical systems did not confirm the existence of this anomaly up to $P \approx 70 \text{ GPa}$.

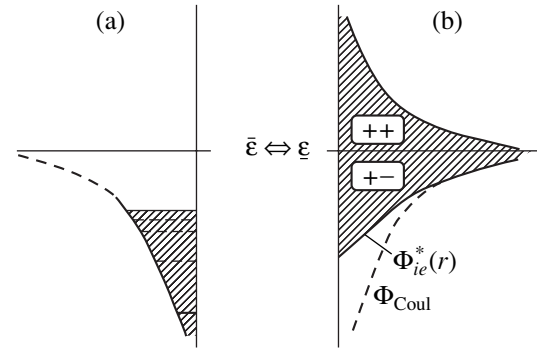


Fig. 14. Glauber-Yukhnovskii electron-ion pseudopotential: (a) bound states and (b) continuous spectrum.

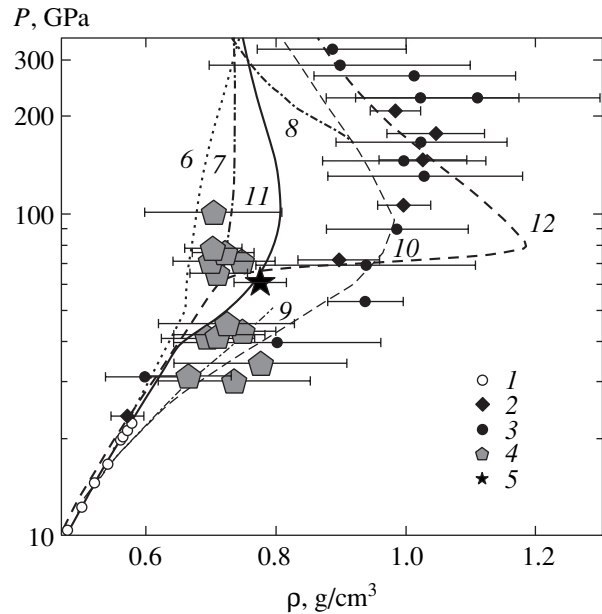


Fig. 15. Shock adiabat curve for deuterium: (1), (2), (3), (4), and (5) experimental data from [34], [31], [32], [33], and [28], respectively; (6), (7), (8), (9), and (10) results of the calculations from [82], [79], [22], [37], and [83], respectively; and (11, 12) results of the present study.

The shock adiabat curves calculated by using the SESAME equation of state [82] (curve 6) do not predict this anomaly in the behavior of shock compressibility, nor does it arise in calculations with semiempirical equations of state [27]. The emergence of this anomaly is not expected either if use is made of *ab initio* approaches, such as the quantum Monte Carlo method [79] (curve 7) and the molecular dynamics method [80]. For deuterium, Ross [83] presented an interpolation equation of state (curve 10) that qualitatively describes experimental results obtained with the aid of lasers.

The approach considered in the present study also does not reproduce this abrupt change in the behavior of the shock adiabat curve for deuterium (toward unexpectedly high degrees of compressibility, $\sigma_{\max} \equiv$

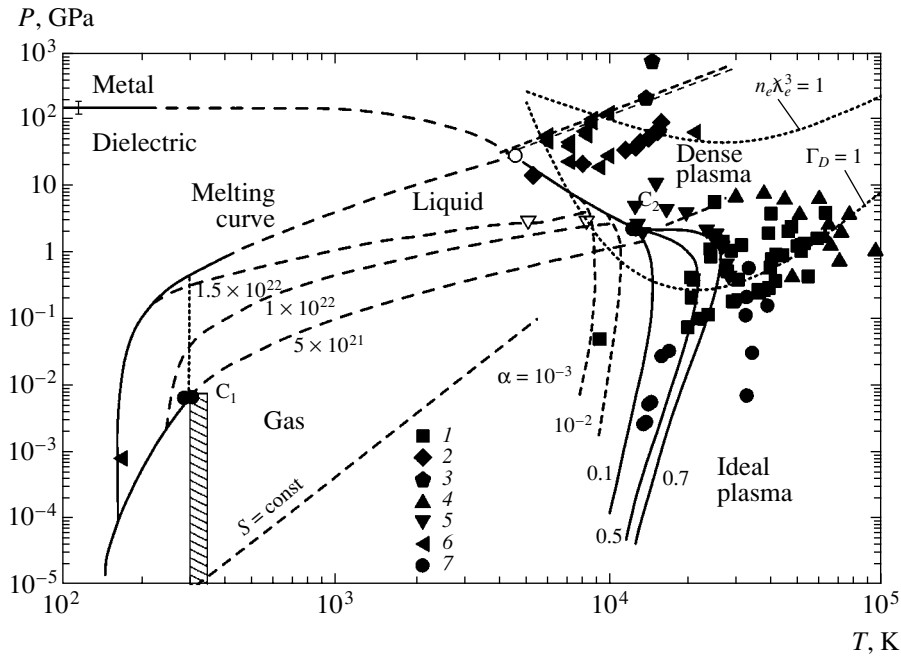


Fig. 16. Phase diagram of xenon. The displayed experimental data were obtained by measuring (i) the equation of state of xenon with the aid of (1) the shock compression of gases in [67], (2) the shock compression of liquids in [49, 85, 86], and (3) quasi-isentropic compression in [49]; (ii) the electrical conductivity in (4) [57, 58], (5) [59], and (6) [41]; and (iii) (7) optical properties in [87].

$\rho_{\max}/\rho_0 \approx 6.5$ versus the expected value of $\sigma_{\max} \approx 4$) in the region $P \approx 0.5\text{--}2$ Mbar (curve *II*), nor does it lead to anomalies for $\rho \geq 1$ g/cm³ that are typical of phase transitions.

The thermodynamics of compressed hydrogen (deuterium) assumes quite a different form if one describes H–H (D–D) interactions by means of the H–H potential introduced in [84] and extensively used in approximate calculations, adopting standard composition rules for H–H₂ interaction. In terms of the soft-sphere-model modification employed in the present study, this corresponds to a much smaller ratio of the intrinsic volumes of H and H₂:

$$\frac{d(H)}{d(H_2)} \approx 0.4 \rightarrow \frac{2v(H)}{v(H_2)} \approx 0.13.$$

For $\rho \geq 0.3$ mol/cm³, this choice of the intrinsic size of an atom immediately leads to “pressure-produced dissociation,” which is accompanied by a dip in the shock adiabatic curve for deuterium (curve *12*).

4.2. Inert Gases

The phase diagram of xenon is shown in Fig. 16. In experiments devoted to measuring the electrical conductivity of xenon under the conditions of multiple shock-wave loads, its density, pressure, and temperatures took values of up to 9.5 g/cm³, 120 GPa, and $(5\text{--}20) \times 10^3$ K, respectively, the electron concentration ranging up to 3×10^{22} cm⁻³ at a degree of ionization less

than or equal to 0.5. In the region of maximum parameter values, the plasma was degenerate ($n_e \lambda_e^3 \sim 50$) and strongly nonideal both with respect to Coulomb ($\Gamma_D \sim 10$) and with respect to interatomic ($\Gamma_a \sim 1$) interaction.

In Fig. 16, the phase boundaries of xenon states are depicted according to [22]. The metallization of xenon under the conditions of static compression at diamond anvils was experimentally observed in [60, 88, 89] at densities of about 12.3 g/cm³ and pressures in the range 130–150 GPa, this being in agreement with the results of the calculations previously performed in [17]. In accordance with the estimates presented in [22], the phase boundary associated with a metal–dielectric transition intersects the line of xenon melting at the triple point (T_{p2}) corresponding to $P \approx 50$ GPa and $T \approx 6000$ K and terminates at critical point C_2 in the plasma region at $P \approx 10$ GPa and $T \approx 10000$ K. At high temperatures, the phase transition is accompanied by a sharp change in the concentration of free electrons in a narrow range of plasma densities, and this is shown in Fig. 16 by the curves corresponding to constant values of the degree of xenon-plasma ionization. A vast body of experimental data obtained from shock-wave experiments in measuring the equation of state for a xenon plasma [3, 49, 67, 85, 86, 90, 91], its optical properties [3, 49, 90, 87], and its electrical conductivity [3, 41, 49, 57–59] furnishes no indications of some of the unusual features in the behavior of xenon in this region of its parameters. The experimental observation of a sharp increase in the electrical conductivity in [41] corre-

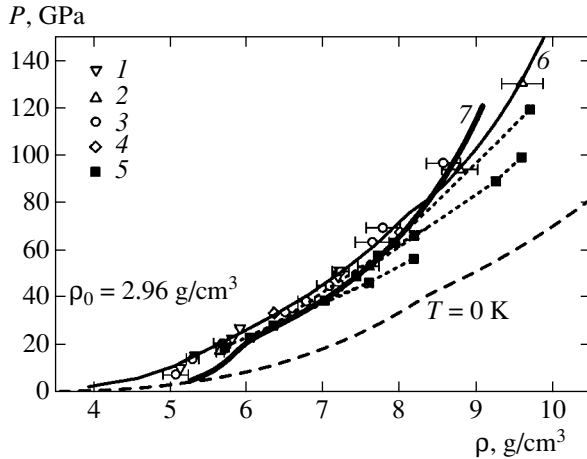


Fig. 17. Shock adiabat curve for xenon. The experimental data were borrowed from (1) [85], (2) [86], (3) [49], (4) [90], and (5) [41]. The displayed theoretical results correspond to the calculations performed (6) in [49] and (7) in the present study (on the shock adiabat for $P = 86.8$ GPa, the characteristic parameters are $T = 29100$ K, $\Gamma_D = 11.9$, $n_e \chi_e^3 = 2.19$, $n_e = 2.63 \times 10^{22} \text{ cm}^{-3}$). The dashed curve represents the “cold” curve from [49].

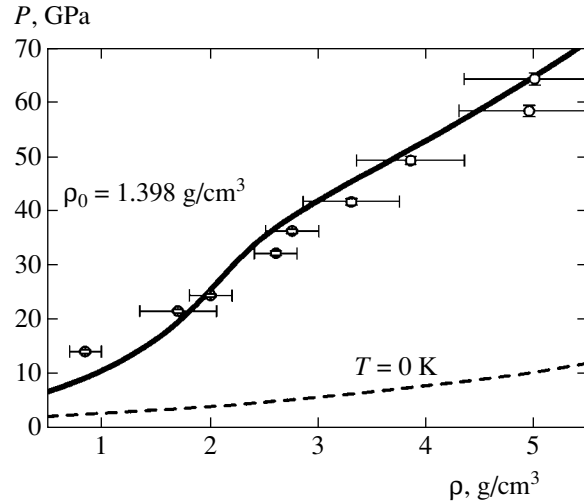


Fig. 18. Shock adiabat curve for argon. The displayed experimental data (points) were borrowed from [92]. The solid curve was calculated in the present study (on the shock adiabat for $P = 54.6$ GPa, the characteristic parameters are $T = 17900$ K, $\Gamma_D = 8.8$, $n_e \chi_e^3 = 0.66$, $n_e = 3.78 \times 10^{21} \text{ cm}^{-3}$). The dashed curve represents the “cold” curve.

sponds to densities of $\rho \approx 8\text{--}10 \text{ g/cm}^3$ and pressures of about 100 GPa.

For shock-compressed plasmas of liquefied inert gases, the radii of the atoms involved were determined by fitting, to the cold curve ($T = 0$ K) for densities of the experimental range (see Table 2), the results of the calculations within the model specified by Eqs. (4.11) and (4.12).

The relationships between the radii of the atoms involved and of their ions of different ionization multiplicities were determined from a calculation of the relevant electron structure in the bounded-atom approximation by the Hartree–Fock method as implemented within the procedure used previously in [74].

We note that, upon a formal interpolation of the melting curve to the parameter region of our interest, some of the experimental points appear to be in the solid phase.

The applicability of the thermodynamic model considered above was tested by comparing the results derived on its basis with experimental data on the shock compression of liquid xenon that were obtained with light-gas guns [85, 86, 90] and in explosive experiments [49] (see Fig. 17). Figure 17 also displays the results of experiments devoted to multiple shock compression [41]. It can be seen that, by and large, the model reproduces experimental results satisfactorily. The discrepancy manifesting itself at low temperatures and pressures may be attributed to an insufficiently accurate approximation of xenon states in the liquid phase. The use of this model makes it possible to obtain a fairly good description of the shock adiabat curves for liquid argon and krypton as well (see Figs. 18, 19).

Here, the displayed experimental data were borrowed from [64, 92].

It should be noted that good agreement could also be reached for the measured values of the brightness temperature and the speed of sound in these substances.

The situation around a thermodynamic description of helium states proves to be more complicated since available experimental data are much scantier and since the helium phase diagram, which is shown in Fig. 20 [22], is quite unusual. The metallization of helium at low temperatures is expected to occur at extremely high pressures of $P \approx 1.1$ TPa. However, plasma phase transitions associated with a sharp change in the ionization composition of helium must take place at much lower pressures. Indeed, the estimates presented in [22] reveal that, with increasing temperature, the melting of solid helium will be accompanied by its direct transition, first, into a singly ionized plasma state (triple point Tp_3) and then into a doubly ionized state (triple point Tp_4). The plasma-phase-transition curves terminate at the critical points C_1 and C_2 , the parameters of the first point ($P \approx 660$ GPa, $T \approx 35000$ K) lying very closely to

Table 2

	s	ε_{SS} , eV	r_{atom}	Q
He	12	0.01354	$2.82a_0$	1
Ar	12	0.0125	$3.2a_0$	1
Kr	12	0.0171	$3.54a_0$	1
Xe	10.5	0.0221	$3.83a_0$	1

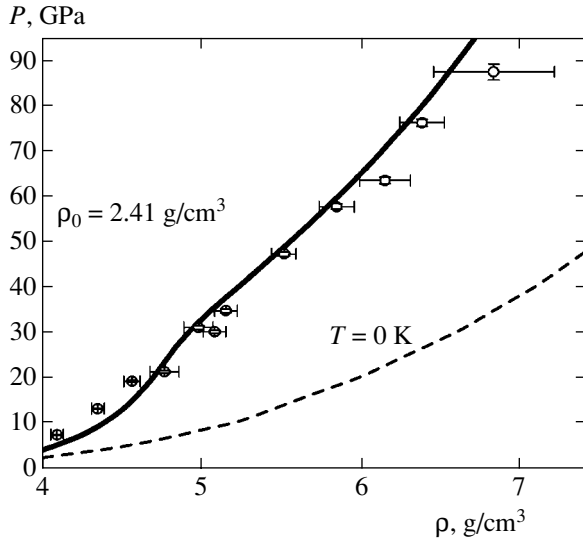


Fig. 19. Shock adiabat curve for krypton. The displayed experimental data (points) were borrowed from [64]. The solid curve was calculated in the present study (on the shock adiabat for $P = 65.8$ GPa, the characteristic parameters are $T = 20100$ K, $\Gamma_D = 8.06$, $n_e \chi_e^3 = 0.66$, $n_e = 4.53 \times 10^{21}$ cm $^{-3}$). The dashed curve represents the “cold” curve.

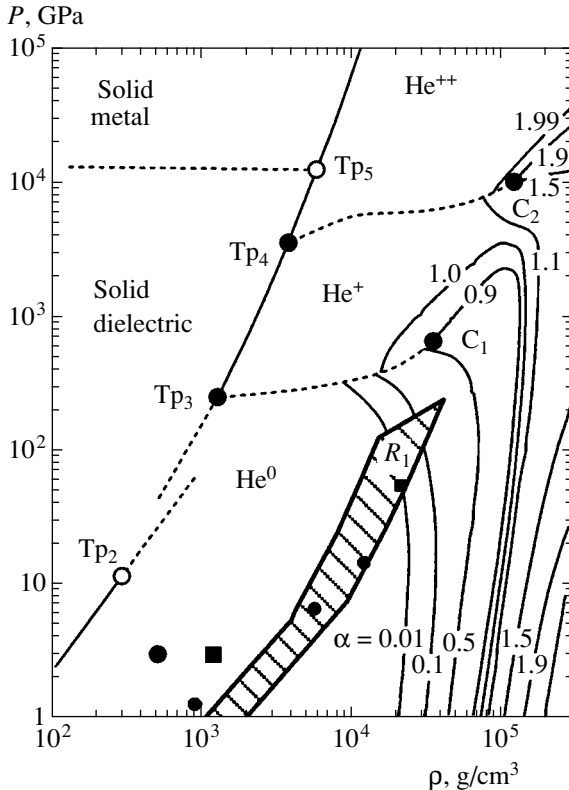


Fig. 20. Phase diagram of helium. The triple points for single and double ionization are denoted by Tp_3 and Tp_4 , respectively. The critical points of plasma phase transitions for single and double ionization are C_1 and C_2 , respectively. The shaded region represents helium states realized in experiments devoted to multiple shock compression [42].

the experimentally accessible region. In Fig. 20, the closed circles and the closed box represent the parameters of helium that were realized in the experiment of Nellis *et al.* [93] in, respectively, the incident and the reflected shock wave. The shaded region corresponds to helium states realized in experiments devoted to multiple shock compression [42]. It should be emphasized that the thermodynamic model satisfactorily describes the data of Nellis *et al.* [93] on the shock compression of helium in the incident and in the reflected shock wave.

5. ELECTRICAL CONDUCTIVITY OF NONIDEAL PLASMAS

In order to describe the electrical conductivity over a broad range of parameters where electrons may obey either Boltzmann or Fermi statistics, expressions (3.1)–(3.4) were combined into an interpolation expression within the τ approximation [94]; that is,

$$\sigma = \frac{4e^2(k_B T)^{-3/2}}{3\sqrt{\pi}m_e} \frac{2}{\chi_e^2} \int_0^\infty \epsilon^{3/2} \tau(\epsilon) \left(-\frac{\partial f_0}{\partial \epsilon} \right) d\epsilon, \quad (5.1)$$

where f_0 is the electron distribution; τ is the relaxation time,

$$\tau^{-1}(\epsilon) = \sqrt{\frac{2\epsilon}{m_e}} \left[\sum_j \gamma_j n_j Q_{ej}(\epsilon) + n_a Q_{ea}(\epsilon) \right],$$

Q_{ea} and Q_{ei} are the transport cross sections for, respectively, electron–atom and electron–ion scattering; and γ_j is a correction for electron–electron scattering. For the case where the change in statistics occurs, this correction was interpolated as [22]

$$\gamma_j = \gamma_j^B - (\gamma_j^B - 1) \frac{T_F}{\sqrt{T_F^2 + T^2}}$$

with T_F being the Fermi temperature and γ_j^B is a correction for the Boltzmann plasma.

In the Born approximation, the cross section for electron scattering on a Coulomb potential is given by

$$Q_{ej} = \frac{Z_j^2 \pi e^4}{\epsilon^2} \Lambda_j, \quad \Lambda_j = \frac{1}{2} \left[\ln(1 + \chi_j) - \frac{\chi_j}{1 + \chi_j} - \frac{Z_j b \chi_j^2}{(1 + \chi_j)^2} \right], \quad (5.2)$$

$$b = \frac{\sum_k Z_k n_k}{\sum_k Z_k^2 n_k + n_e}, \quad \chi_j = \left(\frac{r_{\max j}}{r_{\min j}} \right)^2,$$

where

$$r_{\max j} = \left[4\pi \frac{e^2}{k_B T} \sum_{i=2}^L Z_i^2 n_i + e^2 \left(\frac{\partial n_e}{\partial \mu_e} \right)_T \right]^{-1/2} \quad (5.3)$$

is the Debye screening radius with allowance for electron degeneracy and

$$r_{\min j} = \max \{ Z_j e^2 / 4\epsilon, \chi_e \}$$

is the minimum impact parameter.

In the case of Boltzmann statistics, the expression for Λ_j reduces to the ordinary Coulomb logarithm $\Lambda_j = \ln \chi_j$ in the limit of a weakly nonideal plasma ($\chi_j \gg 1$). For a strongly nonideal plasma ($\chi_j \sim 1$), it proves to be finite, not leading to an nonphysical divergence in the expression for the electrical conductivity, and this gives sufficient grounds to use it in tentative calculations.

Expression (5.1) for the electrical conductivity takes into account the fact that, in the region of high compressions, free electrons are partly or fully degenerate. In this case, the Boltzmann distribution of electrons is replaced by the Fermi–Dirac distribution, the radius of screening being calculated with allowance for electron degeneracy [formula (5.3)]. As a result, the approximation specified by Eq. (5.1) yields Spitzer's asymptotic behavior for a fully ionized Boltzmann plasma. For a full degeneracy of electrons, $\gamma = 1$ and the electrical conductivity tends to expression (3.4), while for a partly ionized plasma, the estimate in (3.1) is valid.

The effect of pressure-produced ionization is the most pronounced in the case of hydrogen (see Fig. 7). In this figure, our data on the quasi-isentropic compression of liquid and gaseous hydrogen in (points 1) planar and (points 2) cylindrical geometries are contrasted against the results of its compression by means of a light-gas gun (points 5) [35], as well as against the results of explosive cylindrical compression by means of an axial magnetic field (points 3 and 4 from [29] and [30], respectively). In view of a light molecular weight, the multiple shock compression of hydrogen is accompanied by a relatively weak heating of this substance—even at maximum pressures of 1 to 10 Mbar, the characteristic values of its temperature do not exceed $T = 10^4$ K and this favors the “cold”-ionization” regime ($k_B T \ll I$). For hydrogen compressed to densities of $\rho \approx 0.01$ – 1.2 g/cm³ and heated to $T \sim 10^4$ K at pressures below 15 Mbar, a wide spectrum of plasma states characterized by a fully developed ionization, $\alpha = 1$, and a high electron concentration of $n_e \approx 2 \times 10^{23}$ cm⁻³ were realized in experiments. At maximum compressions, the plasma in question is degenerate, $n_e \chi_e^3 \approx 200$, and is strongly nonideal both with respect to Coulomb ($\Gamma_D \approx 10$) and to interatomic ($\Gamma_a \approx 1$) interaction.

It is interesting to note that an extrapolation of the simplest plasma models to this region of strong nonideality leads to the thermodynamic instability of Debye–Hückel models (Coulomb collapse)—arrow DC in Fig. 7—and to the divergence of Spitzer's formula—arrow SC. The first of these approximations is depicted by the DHA curve in Fig. 7 and predicts pressure-produced ionization at a density value that is approximately two orders of magnitude lower than its experimental counterpart.

The shock compression of matter leads to the overlap of the wave functions for neighboring atoms and, hence, to the percolation conductivity mechanism [55], which is described in terms of the density-dependent reduction of the ionization potential (curve *P*),

$$\frac{\Delta I}{k_B T} = e^2 \left(\frac{4\pi n}{\zeta} \right)^{1/3}.$$

A decrease in the ionization potential with increasing density is also predicted by the Mott model [5], which was used in [22] to construct a semiempirical wide-range model of ionization equilibrium and transport properties (curve *M* in Fig. 7) of compressed and hot matter; that is,

$$\frac{\Delta I}{k_B T} = -I \ln \left(1 + \exp \left(-2 \frac{R - a(I)}{\Delta(I)} \right) \right).$$

Here, the parameters a , R , and Δ were chosen in such a way as to reproduce experimental data on pressure-produced ionization of alkali metals. It can be seen that the proposed approximations provide a good qualitative description of experimental results.

By using the ring (Debye) approximation in a grand canonical ensemble of statistical mechanics (LDH) to describe Coulomb nonideality, one can reduce the discrepancy between the theoretical and experimental results down to one order of magnitude. The remaining discrepancy can be removed by introducing the hard-sphere model to describe the short-range repulsion of atoms and ions (curve HS) and by taking into account the compression-induced change in the energy spectrum of atoms and ions within a simplified version of the model considered at the beginning of Section 4 (curve CA). An attempt at taking into account the jump-like character of the electrical conductivity in nonideal plasmas was made Redmer *et al.* [56]. The results of their calculations are represented by curve *R* in Fig. 7. The QMC curve corresponds to the calculation of the electrical conductivity by the quantum Monte Carlo method in [24].

Figures 8–11 display the results obtained by studying the electrical conductivity of shock-compressed Xe, Ar, Kr, and He. In just the same way as in the case of hydrogen, one observes here, at “low” temperatures ($k_B T \ll I$), the pressure-produced-ionization effect

occurring at higher plasma densities of $\rho \approx 1\text{--}10\text{ g/cm}^3$. For many-electron atoms, it is also natural to expect that, as compression is increased further, the first ionization induced by pressure will be followed by the next steps of multiple ionization with the emergence of subsequent additional boundaries of phase transitions corresponding to the second and still higher steps of ionization (see Fig. 20). Unfortunately, experimental investigation of these regimes of multiple ionization is presently beyond the capabilities of the explosive experimental equipment that we have at our disposal.

Along with the results of multiple ("cold") compression, Figs. 8–11 exhibit data obtained previously in [57–59] by measuring the electrical conductivity of singly and doubly compressed plasmas. Almost one order of magnitude higher temperatures are realized in experiments with inert gases than in those with hydrogen, the effects of thermal ionization becoming dominant in the former. The role of these effects becomes more pronounced with the increasing molecular weight of the substances being studied, and this is especially spectacular for xenon (see Fig. 8). It can be seen that, upon thermal ionization [$T \approx (2\text{--}10) \times 10^4\text{ K}$], a high level of the electrical conductivity [about $10^3\text{ }(\Omega\text{ cm})^{-1}$] is achieved even at low densities of $\rho < 1\text{ g/cm}^3$; on the other hand, only at extremely high compressions up to densities of $\rho \sim 10\text{ g/cm}^3$ is the same level of electrical conductivity ensured in cold ($T \sim 10^4\text{ K}$) matter under conditions of pressure-produced ionization. It can also be seen that, with increasing molecular weight of substances, the jump in the electrical conductivity due to pressure-produced ionization decreases, falling down to only two orders of magnitude in xenon. It is worthy of note that the values of the electrical conductivity of xenon plasma that were measured in multiple-shock-compression experiments are close to those obtained under static conditions of diamond anvils (the cross in Fig. 8).

It is important to note that some of the models discussed here lose thermodynamic stability in the region of the experiments in question. With some qualifications, this may be considered as an indication of a plasma first-order phase transition leading to the stratification of a strongly nonideal plasma into phases characterized by different degrees of ionization and compressibility [1–4]. A sharp increase in the electrical conductivity of a dense plasma in our experiments suggests the occurrence of such a phase transition.

6. CONCLUSIONS

Thus, we believe that it is necessary to conduct experiments aimed at directly measuring the concentration of free electrons in the region of the possible phase transition. The first studies devoted to such measurements in plasmas have already been performed by the authors.

The chemical model used to describe the equation of state for plasmas in the region of ultrahigh densities yields satisfactory results in this region, which is not traditional for the model in question; nonetheless, the model calls for further refinements associated with taking into account the rearrangement of the internal structure of plasma particles under the conditions of ultradense plasma states.

ACKNOWLEDGMENTS

This work was supported by the Russian Foundation for Basic Research (project nos. 00-15-96738 and 00-02-17550), by the Ministry for Industry and Science of the Russian Federation (state contract no. 40.009.1.1.1192), and by the Presidium of the Russian Academy of Sciences (Interdisciplinary Program for Scientific Research into the Physics and Chemistry of Extreme States of Matter).

REFERENCES

1. *Encyclopedia of Low-Temperature Plasma*, Ed. by V. E. Fortov (Nauka, Moscow, 2000).
2. V. K. Gryaznov, I. L. Iosilevskiĭ, Yu. G. Krasnikov, *et al.*, *Thermal Properties of Working Media of Gas-Phase Nuclear Reactor*, Ed. by V. M. Ievlev (Atomizdat, Moscow, 1980).
3. V. E. Fortov and I. T. Yakubov, *Nonideal Plasma* (Énergoatomizdat, Moscow, 1994).
4. L. D. Landau and Yu. B. Zel'dovich, *Zh. Éksp. Teor. Fiz.* **14**, 32 (1944).
5. N. F. Mott and E. A. Davis, *Electron Processes in Non-Crystalline Materials*, 2nd ed. (Clarendon Press, Oxford, 1979; Mir, Moscow, 1982).
6. F. Hensel and E. U. Frank, *Rev. Mod. Phys.* **40**, 697 (1968).
7. A. G. Barsukov, P. E. Kovrov, V. M. Kuligin, *et al.*, in *Proceedings of 8th IAEA Conference* (1989), Vol. 1, p. 83.
8. V. A. Alekseev and A. A. Vedenov, *Usp. Fiz. Nauk* **102**, 665 (1970) [*Sov. Phys.-Usp.* **13**, 522 (1970)].
9. A. W. DeSilva and J. D. Katsouros, *Phys. Rev. E* **57**, 5945 (1998).
10. A. V. Bushman, B. L. Glushak, V. K. Gryaznov, *et al.*, *Pis'ma Zh. Éksp. Teor. Fiz.* **44**, 375 (1986) [*JETP Lett.* **44**, 480 (1986)].
11. E. G. Maksimov, *Usp. Fiz. Nauk* **169**, 1223 (1999) [*Phys.-Usp.* **42**, 1121 (1999)].
12. E. Wigner and H. B. Huntington, *J. Chem. Phys.* **3**, 764 (1935).
13. A. A. Abrikosov, *Astron. Zh.* **31**, 112 (1954).
14. N. W. Ashcroft, *Phys. Rev. Lett.* **21**, 1748 (1968).
15. E. G. Brovman, Yu. Kogan, and A. Kholac, *Zh. Éksp. Teor. Fiz.* **61**, 2429 (1971) [*Sov. Phys. JETP* **34**, 1300 (1971)].
16. V. P. Trubitsyn, *Fiz. Tverd. Tela* (Leningrad) **8**, 862 (1966) [*Sov. Phys. Solid State* **8**, 688 (1966)].

17. M. Ross and A. K. McMahan, Phys. Rev. B **21**, 1658 (1980).
18. D. A. Young, A. K. McMahan, and M. Ross, Phys. Rev. B **24**, 5119 (1981).
19. J. C. Boettger, Phys. Rev. B **33**, 6788 (1986).
20. K. A. Goettel, J. H. Eggert, I. F. Silvera, and W. C. Moss, Phys. Rev. Lett. **62**, 665 (1989).
21. E. N. Avrorin, B. K. Vodolaga, B. A. Simonenko, and V. E. Fortov, Usp. Fiz. Nauk **163** (5), 1 (1993) [Phys.-Usp. **36**, 337 (1993)].
22. W. Ebeling, A. Förster, V. Fortov, V. Gryaznov, and A. Polishchuk, *Thermophysical Properties of Hot Dense Plasmas* (Teubner, Stuttgart, 1991).
23. D. Saumon and G. Chabrier, Phys. Rev. Lett. **62**, 2397 (1989); D. Saumon and G. Chabrier, Phys. Rev. A **46**, 2084 (1992).
24. I. A. Mulyukov, E. N. Olejnikova, A. L. Khomkin, *et al.*, Phys. Lett. A **289**, 141 (2001).
25. G. É. Norman and A. N. Starostin, Teplofiz. Vys. Temp. **8**, 413 (1970).
26. M. A. Mochalov and O. N. Kuznetsov, in *Abstracts of III Khariton Topical Readings* (Sarov, 2001), p. 108.
27. F. V. Grigor'ev, S. B. Kormer, O. L. Mikhaïlova, *et al.*, Zh. Éksp. Teor. Fiz. **75**, 1683 (1978) [Sov. Phys. JETP **48**, 847 (1978)].
28. S. I. Belov, G. V. Boriskov, A. I. Bykov, *et al.*, Pis'ma Zh. Éksp. Teor. Fiz. **76**, 508 (2002) [JETP Lett. **76**, 433 (2002)].
29. R. S. Hawke, T. J. Burgers, D. E. Duerre, *et al.*, Phys. Rev. Lett. **41**, 994 (1978).
30. A. I. Pavlovskii, G. V. Boriskov, *et al.*, in *Megagauss Technology and Pulsed Power Applications*, Ed. by C. M. Fowler (Plenum, New York and London, 1987).
31. L. B. Da Silva, P. Celliers, G. W. Collins, *et al.*, Phys. Rev. Lett. **78**, 483 (1997).
32. A. N. Mostovych, Y. Chan, T. Lehecha, *et al.*, Phys. Rev. Lett. **85**, 3870 (2000).
33. M. D. Knudsen, D. L. Hanson, J. B. Bailey, *et al.*, Phys. Rev. Lett. **90**, 035505 (2003).
34. N. S. Holmes, M. Ross, and W. J. Nellis, Phys. Rev. B **52**, 15835 (1995).
35. W. J. Nellis, S. T. Weir, and A. C. Mitchell, Rev. High Pressure Sci. Technol. **7**, 870 (1998); S. T. Weir, A. C. Mitchell, and W. J. Nellis, Phys. Rev. Lett. **76**, 1860 (1996).
36. V. E. Fortov, V. Ya. Ternovoï, S. V. Kvitov, *et al.*, Pis'ma Zh. Éksp. Teor. Fiz. **69**, 874 (1999) [JETP Lett. **69**, 926 (1999)]; V. Ya. Ternovoï, A. S. Filimonov, V. E. Fortov, *et al.*, Physica B (Amsterdam) **265**, 6 (1999).
37. D. Beule, W. Ebeling, A. Förster, *et al.*, Phys. Rev. B **59**, 14177 (1999).
38. M. Robnic and W. Kundt, Astron. Astrophys. **120**, 227 (1983).
39. P. Haronska, D. Kremp, *et al.*, Wiss. Z. Wilhelm-Pieck-Univ. Rostock, Naturwiss. Reihe **36**, 98 (1987).
40. W. J. Nellis, Planet. Space Sci. **48**, 671 (2000).
41. V. B. Mintsev, V. Ya. Ternovoï, V. K. Gryaznov, *et al.*, in *Shock Compression of Condensed Matter-1999*, Ed. by S. C. Schmidt, D. P. Dandekar, and J. W. Forbes (Woodbury, New York, 2000), p. 987.
42. V. Ya. Ternovoï, A. S. Filimonov, A. A. Pyalling, *et al.*, in *Shock Compression of Condensed Matter-2001*, Ed. by M. D. Furnish, N. N. Thadhani, and Y. Horie (AIP Press, New York, 2002), p. 107.
43. V. Ya. Ternovoï, in *Nonstationary Problems in Hydrodynamics* (Inst. Gidrodin., Sib. Otd. Akad. Nauk SSSR, 1980), No. 48, p. 141.
44. S. T. Weir, A. C. Mitchell, and W. J. Nellis, J. Appl. Phys. **80**, 1522 (1996).
45. L. M. Barker, T. G. Trucano, J. L. Wize, and J. R. Asay, in *Proceedings of Conference on Shock Waves in Condensed Matter-85* (Plenum, New York, 1986), p. 455.
46. H. Juranek, R. Redmer, G. Roepke, *et al.*, Plasma Phys. **39**, 251 (1999).
47. A. V. Bushman, I. V. Lomonosov, and V. E. Fortov, *Equations of State of Metals at High Energy Densities* (Inst. Probl. Khim. Fiz., Chernogolovka, 1992).
48. I. A. Adamskaya, F. V. Grigor'ev, O. L. Mikhaïlova, *et al.*, Zh. Éksp. Teor. Fiz. **93**, 647 (1987) [Sov. Phys. JETP **66**, 366 (1987)].
49. V. D. Urlin, M. A. Mochalov, and O. L. Mikhailova, High Press. Res. **8**, 595 (1992).
50. V. D. Urlin, M. A. Mochalov, and O. L. Mikhaïlova, Zh. Éksp. Teor. Fiz. **111**, 2099 (1997) [JETP **84**, 1145 (1997)].
51. E. I. Zababakhin, *Mechanics in USSR for 50 Years* (Nauka, Moscow, 1979).
52. A. I. Pavlovskii, G. D. Kuleshov, G. V. Sklizkov, *et al.*, Dokl. Akad. Nauk SSSR **160**, 68 (1965) [Sov. Phys. Dokl. **10**, 30 (1965)].
53. A. A. Brish, M. S. Tarasov, and V. A. Tsukerman, Zh. Éksp. Teor. Fiz. **38**, 22 (1960) [Sov. Phys. JETP **11**, 15 (1960)].
54. V. M. Zamalin, G. É. Norman, and V. S. Filinov, *Monte Carlo Method in Statistical Thermodynamics* (Nauka, Moscow, 1977; Mir, Moscow, 1977).
55. A. A. Likal'ter, Zh. Éksp. Teor. Fiz. **113**, 1094 (1998) [JETP **86**, 598 (1998)].
56. R. Redmer, G. Roepke, S. Kuhlbrodt, and H. Reinholz, Contrib. Plasma Phys. **41**, 163 (2001).
57. Yu. V. Ivanov, V. E. Fortov, V. B. Mintsev, and A. N. Dremin, Zh. Éksp. Teor. Fiz. **71**, 216 (1976) [Sov. Phys. JETP **44**, 112 (1976)].
58. V. B. Mintsev and V. E. Fortov, Pis'ma Zh. Éksp. Teor. Fiz. **30**, 401 (1979) [JETP Lett. **30**, 375 (1979)].
59. V. B. Mintsev, V. E. Fortov, and V. K. Gryaznov, Zh. Éksp. Teor. Fiz. **79**, 116 (1980) [Sov. Phys. JETP **52**, 59 (1980)].
60. M. I. Eremets, E. A. Gregoryanz, V. V. Struzhkin, *et al.*, Phys. Rev. Lett. **85**, 2797 (2000).
61. S. V. Dudin, V. E. Fortov, *et al.*, in *Shock Compression of Condensed Matter-1997*, Ed. by S. C. Schmidt, D. P. Dandekar, and J. W. Forbes (AIP Press, New York, 1998), p. 793.

62. L. A. Gatilov, V. D. Glukhodedov, F. V. Grigor'ev, *et al.*, Prikl. Mekh. Tekh. Fiz., No. 1, 99 (1985).
63. M. I. Dolotenko, A. I. Bykov, *et al.*, in *Megagauss and Megaamper Pulsed Power and Related Topics*, Ed. by V. Chernishev, V. Selimir, and L. Plyashkevitch (VHIEF, Sarov, 1997), p. 805.
64. V. D. Glukhodedov, S. I. Kirshanov, T. S. Lebedeva, and M. A. Mochalov, Zh. Éksp. Teor. Fiz. **116**, 551 (1999) [JETP **89**, 292 (1999)].
65. L. I. Veaser, C. A. Ekdah, H. Oona, *et al.*, in *Abstracts of VIII International Conference on Megagauss Magnetic Field Generation and Related Topics, Tallahassee* (1998), p. 239.
66. K. Seeger, *Semiconductor Physics* (Springer, Berlin, 1974; Mir, Moscow, 1977).
67. V. K. Gryaznov, M. V. Zhernokletov, V. N. Zubarev, *et al.*, Zh. Éksp. Teor. Fiz. **78**, 573 (1980) [Sov. Phys. JETP **51**, 288 (1980)].
68. J. M. Zaiman, *Principles of the Theory of Solids*, 2nd ed. (Cambridge Univ. Press, London, 1972; Mir, Moscow, 1966).
69. W. J. Nellis, S. T. Weir, N. C. Holmes, *et al.*, UCRL-125039, LLNL (1996).
70. V. K. Gryaznov, I. L. Iosilevskii, and V. E. Fortov, Pis'ma Zh. Tekh. Fiz. **8**, 1378 (1982) [Sov. Tech. Phys. Lett. **8**, 592 (1982)].
71. V. K. Gryaznov and V. E. Fortov, Teplofiz. Vys. Temp. **25**, 1208 (1987).
72. V. K. Gryaznov, M. V. Zhernokletov, I. L. Iosilevskii, *et al.*, Zh. Éksp. Teor. Fiz. **114**, 1242 (1998) [JETP **87**, 678 (1998)].
73. I. L. Iosilevskii, Teplofiz. Vys. Temp. **18**, 355 (1980).
74. V. K. Gryaznov, I. L. Iosilevskii, and V. E. Fortov, in *Shock Waves and Extremal States of Substance*, Ed. by V. E. Fortov, L. V. Al'tshuler, R. F. Trunin, and A. I. Funtikov (Nauka, Moscow, 2000).
75. D. A. Young, UCRL-52352, LLNL (1977).
76. A. G. Gaydon and I. R. Hurler, *The Shock Tube in High-Temperature Chemical Physics* (Chapman and Hall, London, 1963; Mir, Moscow, 1966).
77. V. B. Mintsev and V. E. Fortov, Teplofiz. Vys. Temp. **20**, 745 (1982).
78. E. S. Yakub, Teplofiz. Vys. Temp. **28**, 664 (1990); Physica B (Amsterdam) **265**, 31 (1999).
79. C. Pierleoni, D. M. Ceperley, B. Bernu, and W. R. Magro, Phys. Rev. Lett. **73**, 2145 (1994).
80. L. Collins, I. Kwon, J. Kress, *et al.*, Phys. Rev. E **52**, 6202 (1995); S. Günter and A. Kötnies, Phys. Rev. E **55**, 907 (1997).
81. M. Knaup, P. Reinhard, and C. Topffer, Contrib. Plasma Phys. **39**, 57 (1999).
82. G. I. Kerley, in *Theoretical Equation of State for Deuterium* (National Technical Information Service, Springfield, VA, 1972), NTIS Document No. LA-47766.
83. M. Ross, Phys. Rev. B **58**, 669 (1998).
84. F. Ree, M. Ross, and D. Young, J. Chem. Phys. **79**, 1487 (1983).
85. R. Keeler, M. Van Thiel, and B. Alder, Physica (Amsterdam) **31**, 1437 (1965).
86. W. Nellis, M. Van Thiel, and A. Mitchel, Phys. Rev. Lett. **48**, 816 (1982).
87. M. I. Kulish, V. K. Gryaznov, V. B. Mintsev, *et al.*, Teplofiz. Vys. Temp. **33**, 967 (1995).
88. K. A. Goettel, J. H. Eggert, I. F. Silvera, and W. C. Moss, Phys. Rev. Lett. **62**, 665 (1989).
89. R. Reichlin, K. E. Brister, A. K. McMahan, *et al.*, Phys. Rev. Lett. **62**, 669 (1989).
90. H. B. Radousky and M. Ross, Phys. Lett. A **129**, 43 (1988).
91. V. E. Fortov, V. K. Gryaznov, V. B. Mintsev, *et al.*, Contrib. Plasma Phys. **41**, 215 (2001).
92. F. V. Grigor'ev, S. B. Kormer, O. L. Mikhaïlova, *et al.*, Zh. Éksp. Teor. Fiz. **88**, 1271 (1985) [Sov. Phys. JETP **61**, 751 (1985)].
93. W. J. Nellis, N. C. Holmes, A. C. Mitchell, *et al.*, Phys. Rev. Lett. **53**, 1248 (1984).
94. V. K. Gryaznov, Yu. V. Ivanov, A. N. Starostin, and V. E. Fortov, Teplofiz. Vys. Temp. **14**, 643 (1976).

Translated by A. Isaakyan